

Contents lists available at ScienceDirect

# Comput. Methods Appl. Mech. Engrg.

journal homepage: www.elsevier.com/locate/cma





# Phase-field description of fracture in NiTi single crystals

D. Kavvadias, Th. Baxevanis\*

Department of Mechanical Engineering, University of Houston, Houston, TX 77204-4006, USA

#### ARTICLE INFO

Keywords:
Phase-field approach to fracture
NiTi
Shape memory alloys
Single crystals
Finite element analysis

#### ABSTRACT

A phase-field model for thermomechanically-induced fracture in NiTi at the single crystal level, i.e., fracture under loading paths that may take advantage of either of the functional properties of NiTi-superelasticity or shape memory effect-, is presented, formulated within the kinematically linear regime. The model accounts for reversible phase transformation from austenite to martensite habit plane variants and plastic deformation in the austenite phase. Transformation-induced plastic deformation is viewed as a mechanism for accommodation of the local deformation incompatibility at the austenite-martensite interfaces and is accounted for by introducing an interaction term in the free energy derived based on the Mori-Tanaka and Kröner micromechanical assumptions and the hypothesis of martensite instantaneous growth within austenite. Based on experimental observations suggesting that NiTi fractures in a stress-controlled manner, damage is assumed to be driven by the elastic energy, i.e., phase transformation and plastic deformation are assumed to contribute in crack formation and growth indirectly through stress redistribution. The model is restricted to quasistatic mechanical loading (no latent heat effects), thermal loading sufficiently slow with respect to the time rate of heat transfer by conduction (no thermal gradients), and a temperature range below  $M_d$ , which is the temperature above which the austenite phase is stable, i.e., stress-induced martensitic transformation is suppressed. The numerical implementation of the model is based on an efficient scheme of viscous regularization in both phase transformation and plastic deformation, an explicit numerical integration via a tangent modulus method, and a staggered scheme for the coupling of the unknown fields. The model is shown able to capture transformation-induced toughening, i.e., stable crack advance attributed to the shielding effect of inelastic deformation left in the wake of the growing crack under nominal isothermal loading, actuation-induced fracture under a constant bias load, and crystallographic dependence on crack pattern.

#### 1. Introduction

Since its discovery in 1963, NiTi has attracted significant interest due to its unique functional properties combined with good processability, corrosion and wear resistance, and biocompatibility. NiTi belongs to a class of materials named Shape Memory Alloys (SMAs), which in general exhibit a diffusionless, solid-to-solid, phase transformation of their crystal structure from austenite to martensite. Forward phase transformation from austenite to martensite results in large strain accommodation, which can be almost completely recovered during reverse phase transformation, triggered by unloading (superelastic effect) or unloading followed by heating (shape memory effect). The above functional properties of NiTi renders it desirable in a wide range of applications, from biomedical stents to solid-state actuators, elastocaloric cooling, robotics, and consumer electronics [1,2]. However, NiTi is prone to failure, and, therefore, to fulfill the necessary reliability and safety requirements of applications, the NiTi's fatigue and overload

E-mail addresses: dkavvadi@uh.edu (D. Kavvadias), tbaxevanis@uh.edu (T. Baxevanis).

<sup>\*</sup> Corresponding author.

fracture response has become a topic of great technological importance. Although polycrystalline NiTi is primary in commercial use today, single crystal fracture response provides insight into the coupling of crack formation and growth kinetics with the operant deformation mechanisms, and, potentially, with grain sizes and boundaries, and texture.

NiTi belongs to a relatively brittle class of materials, that of intermetallics, and fails by cleavage of crystallographic planes, which, depending on the local precipitate size and concentration, is assisted by ductile tearing [3,4]. Ni-rich NiTi alloys are generally heat treated to produce metastable  $Ni_4Ti_3$  precipitates of large volume fractions, estimated around  $2 \sim 7\%$  depending on aging. Decreasing  $Ni_4Ti_3$  precipitate size results in a less ductile response and fewer dimples on the fracture surface. Nevertheless, both experimental observations [4] and numerical simulations [5] suggest that the work expended on the *intrinsic* damage mechanisms of void nucleation and growth has a minor contribution to the work balance during crack growth, which is stress-driven. *Extrinsic* shielding resulting from inelastic deformation left in the wake of the advancing crack results in toughness enhancement during crack advance, *i.e.*, slow and stable crack extension [6], similarly to ductile materials. Transformation from austenite to martensite [7–11], and *vice versa* [12], (re)orientation of martensite variants [13], overload and transformation-induced plasticity [10,13–15], and thermomechanical coupling associated to latent heat [16–18] have an impact on the toughness enhancement observed. Large-scale phase transformation in front of a crack, resulted, for example, due to thermal actuation, promotes crack advance, counteracting the aforementioned stabilizing effect of the irrecoverable deformation left in the crack's wake [15,19,20].

Regarding the NiTi's fracture response at the single crystal level. Creuziger et al. [21] conducted fracture experiments of notched NiTi single crystal tension specimens with crystallographic directions [100] and [111] along, the perpendicular to the notch plane, tensile axis. The distinct feature of crystals is the orientation dependence of the activation of the crystallographic deformation mechanisms, i.e., martensitic transformation, dislocations, and deformation twins in the case of NiTi, which induces orientation dependent mechanical anisotropy. In the [100] notched sample, the crack that initiated first was arrested prior to the initiation of the second crack, which propagated stably through nearly the entire width of the sample on the notch plane. The [111] notched sample underwent unstable fracture and although the crack appears to have initially propagated on the plane of the notch from the tip of the notch, its path quickly deviated by over 25° from the notch plane before returning to it. Pauses in crack propagation, initial crack growth arrest, kinking and branching are believed to be a result of TiC precipitates and not significant in comparison to the overall stable crack growth observed. Crack kinking was evident in fracture experiments performed in CuAlNi single crystals, in which straight cracks with fixed direction were observed to propagate either stably or unstably at directions forming angles between -50° to 43° with the notch plane depending on the crystallographic orientation [22]. These angles cannot be explained by crack direction criteria for a single phase cubic material, i.e., a non-transforming material, as crack kinking under "Mode I" symmetric loading in the absence of transformation is predicted only for values of  $E_{11}/E_{22}$  greater than 1 [23];  $E_{11}$  is the elastic modulus in the direction of the notch axis and  $E_{22}$  in the loading axis. Thus, the fracture direction is strongly tied to microstructure formation, i.e., transformation, in these SMAs. It should be noted, however, that phase transformation may not have a similar impact on the fracture direction in NiTi due to the different crystal structure and types of transformation that occur in these alloys resulting in vast larger number (192) of possible martensite plates that can be formed.

The aim, herein, is to develop a phenomenological phase-field model for fracture in NiTi single crystals. The proposed model is developed by coupling a micromechanics-based constitutive model for the deformation response of NiTi at the single crystal level with the phase-field approach to fracture. The major advantage of the phase-field approach over discrete fracture models lies on its ability to model crack nucleation, propagation, merging, and branching without *ad hoc* additions to the theory and without adaptive mesh refinement for sufficiently fine mesh resolutions. This stems from the regularization of the sharp crack surface topology by a diffusive crack zone governed by a scalar auxiliary variable, a phase field, which interpolates between the unbroken and the broken state of the material. In the phase-field approach to fracture, also known as variational approach to fracture, the solution to the fracture problem is found as the minimizer of a global energy functional that includes a volumetric approximation of total fracture energy. The phase-field approach to fracture has been focused mostly on brittle materials at the macroscopic level [24–26] with proposed modifications to fracture in ductile materials [27–29], geomaterials [30,31], composites [32,33], rubbery polymers [34], hydrogen embrittlement [35], hydraulic fracturing [36], and recently extended to fatigue as well [37–41]. Relevant to the current study, the phase-field approach to fracture was employed to SMAs at the polycrystalline level [42,43] and to face centered cubic single crystals of conventional metals [44–49].

The proposed model includes a 3D, micromechanics-based, description of the deformation response of NiTi, including a description of transformation-induced plasticity as a mechanism for accommodation of the deformation incompatibility at the austenite-martensite interface. The model accounts for reversible phase transformation from austenite to martensite and dislocation slipping in the austenite state, neglecting martensite variant reorientation, detwinning, and deformation twinning in martensite (a brief review of the deformation mechanisms in NiTi is provided below). The model adopts a single value for the energy expended to create new surfaces, which corresponds to the fracture toughness of stress-induced martensite – of a rather complex, twinned microstructure – in the fully-transformed zone near the crack tip. Thus, the model is applicable for temperatures below  $M_d$ , i.e., the highest temperature above which martensite can no longer be stress-induced, since, as recently shown in [5,50], the fracture toughness of SMAs is piece-wise constant with respect to temperature, below and above  $M_d$ , with the value below  $M_d$  corresponding to the fracture toughness of martensite and that above corresponding to austenite. The model further assumes that inelastic deformation associated with phase transformation and plastic deformation contributes to the fracture response only through stress redistribution, underpinning the experimental/numerical evidence that the fracture process in SMA is stress-driven [4,5].

The paper is structured as follows. A brief overview of the deformation mechanisms in NiTi single crystals is provided in Section 2. The governing equations of the proposed subgranular phase-field approach to fracture in NiTi are outlined in Section 3. In Section 4, the finite-element implementation of the model is described. In Section 5, numerical examples and presented and discussed and, lastly, conclusions are drawn in Section 6.

#### 2. Deformation mechanisms in NiTi single crystals

In NiTi, austenite, which is characterized by a cubic B2 crystallographic structure, transforms into 12 monoclinic martensite variants (B19' crystallographic structure) by mechanical loading and/or cooling, during which chemical composition remains unaltered while the atoms are organized in a new crystallographic lattice (non-diffusive, first-order phase transition). The martensite phase is formed as thin platelets, needles, or laths within the austenite parent phase with the two phases fitting together along planes, called *invariant* or *habit* planes, that remain unchanged, *i.e.*, neither deform nor rotate. These planes/interfaces are between austenite and twins of martensite variants, called *Habit Plane Variants* (HPVs), that comprise of two *Lattice Correspondent Variants* (LCVs). Crystallographic theory predicts 192 HPVs, *i.e.*, 192 possible distinct interfaces between austenite and martensite [51]. Movement of interfaces between HPVs is referred to as HPV *reorientation*, and movement of interfaces between LCVs as *detwinning*. Plastic deformation in austenite is strongly influenced by  $\langle 100 \rangle \{011\}$  and  $\langle 101 \rangle \{001\}$  slip modes and, as recently observed, by  $\langle 111 \rangle \{110\} [52]$ . Dislocation slipping is observed even if the overall applied stress is lower than the yield stress of austenite as a mechanism to accommodate the deformation incompatibility at the austenite interfaces. The plastic deformation in martensite is mainly due to twin activity, 11 possible twinning systems were pointed out by [54], while only one slip system (001)[100] exists due to the low symmetry of the martensite monoclinic crystal structure.

## 3. Phase-field model for the fracture response of single NiTi crystals

The adopted single crystal model accounts for reversible phase transformation from austenite to HPVs, dislocation slipping in the austenite state, and elastic anisotropy for the two phases [55]. The interaction between the two phases is described by a mean-field approach through the Eshelby tensor by regarding the HPVs as ellipsoidal inclusions embedded in the austenite matrix in order to reflect the internal stress states that can activate dislocation slipping, *i.e.*, TRIP, even for applied load levels that are not high enough to do so otherwise [56].

#### 3.1. Kinematics

The inelastic deformation of an SMA crystal is defined as an average over a Representative Volume Element (RVE), which should be large enough to include a sizable set of martensite HPVs and slip systems within a single crystal austenite. It is further assumed that the austenite–martensite formed interfaces are coherent and their motion along with the dislocation motion is rate-independent.

Assuming small strains, the total macroscopic strain tensor

$$\mathbf{\varepsilon} = \mathbf{\varepsilon}^e + \mathbf{\varepsilon}^t + \mathbf{\varepsilon}^p,\tag{1}$$

is additively decomposed to elastic,  $\mathbf{\epsilon}^e$ , transformation,  $\mathbf{\epsilon}^t$ , and plastic,  $\mathbf{\epsilon}^p$ , strain tensors. Thermal strain, which is an order of magnitude smaller than the transformation strain, is not included for simplicity; its proper implementation in a single crystal model is not trivial [57,58] given the highly anisotropic thermal expansion of the monoclinic martensite variants [59].

## 3.1.1. Transformation strain

By the rule of mixtures, the transformation strain can be written as

$$\mathbf{\varepsilon}^t = \sum_{\alpha=1}^{N_t} \widehat{\mathbf{\varepsilon}}_t^{(\alpha)} \xi^{(\alpha)},\tag{2}$$

where  $\hat{\mathbf{E}}_t^{(\alpha)} = \frac{1}{2} g_t \left( \mathbf{I}^{(\alpha)} \otimes \mathbf{d}^{(\alpha)} + \mathbf{d}^{(\alpha)} \otimes \mathbf{I}^{(\alpha)} \right)$ ,  $\mathbf{I}^{(\alpha)}$ ,  $\mathbf{d}^{(\alpha)}$ , and  $g_t$  are the stress free transformation strain, the habit plane normal, the transformation direction, and the magnitude of transformation, respectively, for each of the  $N_t$  martensite HPVs, given by crystallography considerations, and  $\xi^{(\alpha)}$ , restricted by  $0 \le \xi^{(\alpha)} \le 1$ , stands for the volume fraction of martensite corresponding to the  $\alpha_{\text{th}}$ -HPV system in an RVE. The total volume fraction of martensite,  $\xi = \sum_{\alpha} \xi^{(\alpha)}$ , must also lie in the range  $0 \le \xi \le 1$ .

The rate of  $\mathbf{\varepsilon}^t$  thus reads as

$$\dot{\mathbf{\epsilon}}^t = \sum_{\alpha=1}^{N_t} \widehat{\mathbf{\epsilon}}_t^{(\alpha)} \dot{\xi}^{(\alpha)}. \tag{3}$$

## 3.1.2. Plastic strain

The overall plastic strain tensor can be similarly written by the rule of mixtures as

$$\boldsymbol{\varepsilon}^{p} = (1 - \xi)\boldsymbol{\varepsilon}_{A}^{p} + \sum_{\alpha=1}^{N_{t}} \xi^{(\alpha)} \boldsymbol{\varepsilon}_{M_{(\alpha)}}^{p}, \tag{4}$$

where  $\mathbf{\epsilon}_A^p$  and  $\mathbf{\epsilon}_{M_{(a)}}^p$  stand for the plastic strain tensors in the regions occupied by austenite and  $\alpha_{\mathrm{th}}$ -martensite HPV, respectively.

The rate of  $\mathbf{\epsilon}^p$  is thus given as

$$\dot{\boldsymbol{\varepsilon}}^{p} = (1 - \xi)\dot{\boldsymbol{\varepsilon}}_{A}^{p} + \sum_{\alpha=1}^{N_{t}} \xi^{(\alpha)}\dot{\boldsymbol{\varepsilon}}_{M_{(\alpha)}}^{p} - \sum_{\alpha=1}^{N_{t}} \dot{\boldsymbol{\xi}}^{(\alpha)} \left(\boldsymbol{\varepsilon}_{A}^{p} - \boldsymbol{\varepsilon}_{M_{(\alpha)}}^{p}\right) \\
= (1 - \xi) \left[\dot{\boldsymbol{\varepsilon}}_{A}^{p} - \sum_{\alpha=1}^{N_{t}} \frac{\dot{\boldsymbol{\xi}}^{(\alpha)}}{1 - \xi} \left(\boldsymbol{\varepsilon}_{A}^{p} - \boldsymbol{\varepsilon}_{M_{(\alpha)}}^{p}\right)\right] + \sum_{\alpha=1}^{N_{t}} \boldsymbol{\xi}^{(\alpha)} \left[\dot{\boldsymbol{\varepsilon}}_{M_{(\alpha)}}^{p} - \frac{\dot{\boldsymbol{\xi}}^{(\alpha)}}{\boldsymbol{\xi}^{(\alpha)}} \left(\boldsymbol{\varepsilon}_{A}^{p} - \boldsymbol{\varepsilon}_{M_{(\alpha)}}^{p}\right)\right].$$
(5)

The rate of  $\mathbf{\epsilon}^p$  can moreover be described by crystallographic slip mechanisms in the austenite phase

$$\dot{\boldsymbol{\varepsilon}}^p = (1 - \xi) \sum_{l=1}^{N_A} \hat{\boldsymbol{\varepsilon}}_p^{(l)} \dot{\boldsymbol{\gamma}}_A^{(l)},\tag{6}$$

where  ${}_{A}\widehat{\mathbf{c}}_{p}^{(l)} = \frac{1}{2} \left( \mathbf{q}_{A}^{(l)} \otimes \mathbf{r}_{A}^{(l)} + \mathbf{r}_{A}^{(l)} \otimes \mathbf{q}_{A}^{(l)} \right)$  is the orientation tensor of the  $l_{\text{th}}$ -slipping system of austenite,  $\mathbf{q}_{A}^{(l)}$ ,  $\dot{\mathbf{r}}_{A}^{(l)}$ ,  $\dot{\mathbf{r}}_{A}^{(l)}$ ,  $\dot{\mathbf{r}}_{A}^{(l)}$  are the respective shear direction, slip plane normal, and average shearing rate, respectively, and  $N_{A}$  denotes the number of slip systems.

Eqns (5) and (6), which hold for every  $\xi^{(\alpha)}$ ,  $\alpha = 1, ..., N_t$ , yield

$$\begin{cases} \dot{\boldsymbol{\varepsilon}}_{A}^{p} = \sum_{\alpha=1}^{N_{t}} \frac{\dot{\boldsymbol{\varepsilon}}^{(\alpha)}}{1 - \dot{\boldsymbol{\varepsilon}}} \left( \boldsymbol{\varepsilon}_{A}^{p} - \boldsymbol{\varepsilon}_{M_{(\alpha)}}^{p} \right) + \sum_{l=1}^{N_{A}} A \widehat{\boldsymbol{\varepsilon}}_{p}^{(l)} \dot{\boldsymbol{\gamma}}_{A}^{(l)}, \\ \dot{\boldsymbol{\varepsilon}}_{M_{(\alpha)}}^{p} = \frac{\dot{\boldsymbol{\varepsilon}}^{(\alpha)}}{\boldsymbol{\varepsilon}^{(\alpha)}} \left( \boldsymbol{\varepsilon}_{A}^{p} - \boldsymbol{\varepsilon}_{M_{(\alpha)}}^{p} \right). \end{cases}$$

$$(7)$$

Thus, the rates of plastic strain in the austenite and  $\alpha_{\text{th}}$ -martensite HPV are dependent on the dislocation slip rates on austenite's slip systems and on the rates of expansion/shrinkage of the HPVs, thus, the model accounts for the inheritance of plastic strain from one phase to another.

## 3.2. Balance laws and entropy inequality principle

The phase-field model for fracture in NiTi single crystals is derived by postulating a *microforce balance* in addition to the usual balance laws and entropy inequality principle [60].

The local forms of the postulated balance laws are derived from their respective global forms, given below, which hold for all subregions  $\mathcal{B}$  of the continuum body,  $\mathcal{Q}$ , with a sufficiently smooth boundary  $\partial \mathcal{B}$ . All integrands are at least  $C^0$ -continuous.

## 3.2.1. Balance of linear momentum (equilibrium)

$$\int_{\partial B} \mathbf{\sigma} \cdot \mathbf{n} \, ds + \int_{B} \mathbf{b} \, d\mathbf{x} = 0 \Rightarrow \mathbf{\nabla} \cdot \mathbf{\sigma} + \mathbf{b} = 0,$$
(8)

where  $\sigma$  is the Cauchy stress, **b** the body force per unit volume, and  $\nabla$  is the differential nabla operator.

## 3.2.2. Balance of angular momentum

$$\int_{\partial B} \mathbf{r} \times (\mathbf{\sigma} \cdot \mathbf{n}) \, ds + \int_{B} \mathbf{r} \times \mathbf{b} \, dx = 0 \Rightarrow \mathbf{\sigma} = \mathbf{\sigma}^{T}, \tag{9}$$

where  $\mathbf{n}$  the outward unit normal of  $\partial \mathcal{B}$ ,  $\mathbf{r}$  the position vector of a material point, and  $\times$  denotes the cross product between two vectors.

#### 3.2.3. Microforce balance

Following [60], the balance of a microforce system is postulated

$$\int_{\partial \mathcal{B}} \zeta \cdot \mathbf{n} \, ds + \int_{\mathcal{B}} \pi \, d\mathbf{x} = 0 \Rightarrow \nabla \cdot \zeta + \pi = 0,\tag{10}$$

where  $\pi$  is an internal scalar microforce and  $\zeta$  a vector stress that exerts a scalar traction  $\zeta \cdot \mathbf{n}$  on  $\partial \mathcal{B}$ .

## 3.2.4. Energy balance

The energy balance is stated as

$$\int_{B} \dot{u} \, d\mathbf{x} = \int_{\partial B} \mathbf{t} \cdot \dot{\mathbf{u}} \, ds + \int_{B} \mathbf{b} \cdot \dot{\mathbf{u}} \, d\mathbf{x} + \int_{\partial B} (\boldsymbol{\zeta} \cdot \mathbf{n}) \dot{c} \, ds + \int_{B} r \, d\mathbf{x} - \int_{\partial B} \mathbf{q} \cdot \mathbf{n} \, ds$$

$$\stackrel{(10)}{\Rightarrow} \dot{u} = \mathbf{\sigma} : \dot{\mathbf{\epsilon}} + \boldsymbol{\zeta} \cdot \boldsymbol{\nabla} \dot{c} - \pi \dot{c} + r - \boldsymbol{\nabla} \cdot \mathbf{q}, \tag{11}$$

where u is the internal energy per unit volume, u is the displacement vector, c is the phase-field parameter (or order parameter) to be further defined below,  $\mathbf{q}$  is the heat flux, and r is a heat source.

Under the assumptions r = 0 and  $\nabla \cdot \mathbf{q} = \mathbf{0}$ , the above equation simplifies to

$$\dot{u} = \mathbf{\sigma} : \dot{\mathbf{\epsilon}} + \mathbf{\zeta} \cdot \nabla \dot{c} - \pi \dot{c}.$$
 (12)

#### 3.2.5. Entropy inequality principle

Under the above assumptions, the second law of thermodynamics reads as

$$\int_{\mathcal{B}} \dot{s} d\mathbf{x} \ge -\int_{\partial \mathcal{B}} \frac{\mathbf{q} \cdot \mathbf{n}}{T} ds \Rightarrow \dot{s} \ge \frac{\mathbf{q} \cdot \nabla T}{T^2},$$

where s is the entropy per unit mass density and T is the absolute temperature.

Assuming  $\nabla T = 0$ , the entropy inequality principle can be stated in terms of dissipation, D, as

$$D = \dot{s}T > 0, \tag{13}$$

In view of the energy balance equation (12) and the Legendre transformation,

$$u = \psi + Ts, \tag{14}$$

where  $\psi$  is the Helmholtz free energy, the dissipation inequality can be further stated as

$$D = \mathbf{\sigma} : \dot{\mathbf{\epsilon}} - s\dot{T} + \mathbf{\zeta} \cdot \nabla \dot{c} - \pi \dot{c} - \dot{\psi} \ge 0. \tag{15}$$

The assumption of a uniform throughout the material, at every instant, temperature distribution,  $\nabla T = 0$ , corresponds to assuming the rate of both the mechanical and thermal loading being sufficiently slow with respect to the time rate of heat transfer by conduction.

#### 3.3. Constitutive response

Given the balance equations, the constitutive equations can now be derived in a thermodynamically consistent manner by postulating the Helmholtz free energy.

### 3.3.1. Helmholtz free energy

Following the choice of the applied strain tensor  $\varepsilon$  and absolute temperature T as external state variables, the Helmholtz free energy per unit reference volume is taken to be

$$\psi\left(\boldsymbol{\varepsilon},T,\boldsymbol{\xi}^{(\alpha)},\boldsymbol{\gamma}_{A}^{(l)},c,\boldsymbol{\nabla}c\right)=\psi_{el}\left(\boldsymbol{\varepsilon},T,\boldsymbol{\xi}^{(\alpha)},\boldsymbol{\gamma}_{A}^{(l)}\right)+\psi_{int}\left(\boldsymbol{\varepsilon},T,\boldsymbol{\xi}^{(\alpha)},\boldsymbol{\gamma}_{A}^{(l)}\right)+\psi_{ch}\left(T,\boldsymbol{\xi}^{(\alpha)}\right)+\psi_{fr}\left(c,\boldsymbol{\nabla}c\right),$$

where the various contributions are described below.

Elastic energy.- The elastic contribution on the free energy is postulated as

$$\psi_{el}\left(\mathbf{\varepsilon}, T, \xi^{(\alpha)}, \gamma_A^{(l)}\right) = g(c)W_{el}^{+}\left(\mathbf{\varepsilon}, T, \xi^{(\alpha)}, \gamma_A^{(l)}\right) + W_{el}^{-}\left(\mathbf{\varepsilon}, T, \xi^{(\alpha)}, \gamma_A^{(l)}\right),\tag{16}$$

where

$$W_{el}^{+} = \left(C_{11} + \frac{C_{12}}{6}\right) \left\langle \text{tr}(\mathbf{\epsilon}^{e})\right\rangle_{+}^{2} + C_{44} \left(\mathbf{\epsilon}_{dev}^{e} : \mathbf{\epsilon}_{dev}^{e}\right) + \left(\frac{C_{11} - C_{12}}{2} - C_{44}\right) \sum_{r=1}^{3} \left(\bar{\epsilon}_{dev,rr}^{e}\right)^{2}, \tag{17}$$

and

$$\mathbf{W}_{el}^{-} = \left(C_{11} + \frac{C_{12}}{6}\right) \left\langle \operatorname{tr}(\mathbf{\varepsilon}^{e})\right\rangle_{-}^{2}. \tag{18}$$

In the above, the notation  $\langle \alpha \rangle_{\pm} = \frac{1}{2} (\alpha \pm |\alpha|)$  denotes the positive and negative parts of an expression  $\alpha$ ,  $\mathfrak{E}^e_{dev}$  is the deviatoric part of the elastic strain tensor, i.e.,  $\mathfrak{E}^e_{dev} := \mathfrak{E}^e - \mathfrak{E}^e_{vol}$ , where  $\mathfrak{E}^e_{vol} := \frac{1}{3} \operatorname{tr}(\mathfrak{E}^e) \delta$  is the volumetric elastic strain tensor and  $\delta$  is the unit tensor with components  $\delta_{ij} = 1$  if i = j and  $\delta_{ij} = 0$  if  $i \neq j$ ,  $C_{11}$ ,  $C_{12}$ , and  $C_{44}$  are elastic constants of the fourth-order elasticity tensor  $C_{ijkl} = C_{12}\delta_{ij}\delta_{kl} + C_{44} \left(\delta_{ik}\delta_{jl} + \delta_{il}\delta_{jk}\right) + \left(C_{11} - C_{12} - 2C_{44}\right)\delta_{ijkl}$  of austenite in the reference system of the cubic crystal unit cell of austenite, where  $\delta_{ijkl} = 1$  if i = j = k = l and  $\delta_{ijkl} = 0$  otherwise,  $\bar{\mathfrak{E}}^e := \mathbf{R} \mathbf{E}^e \mathbf{R}^T$ , where  $\mathbf{R} = \mathbf{\Theta}_3 \mathbf{\Theta}_2 \mathbf{\Theta}_1$  is the rotation matrix between the reference system of the crystal unit cell and the fixed orthonormal reference frame,

$$\Theta_{1} = \begin{bmatrix}
\cos \theta_{1} & \sin \theta_{1} & 0 \\
-\sin \theta_{1} & \cos \theta_{1} & 0 \\
0 & 0 & 1
\end{bmatrix}, \quad
\Theta_{2} = \begin{bmatrix}
\cos \theta_{2} & 1 & -\sin \theta_{2} \\
0 & 1 & 0 \\
\sin \theta_{2} & 0 & \cos \theta_{2}
\end{bmatrix}, \quad
\Theta_{3} = \begin{bmatrix}
\cos \theta_{3} & \sin \theta_{3} & 0 \\
-\sin \theta_{3} & \cos \theta_{3} & 0 \\
0 & 0 & 1
\end{bmatrix}, \tag{19}$$

 $\{\theta_1, \theta_2, \theta_3\}$  are the Euler angles, and g(c) is a degradation function such that  $0 \le g(c) \le 1$ , g(0) = 1, g(1) = 0, and g'(c) < 0, where the prime denotes differentiation with respect to argument. Note that the effective stiffness tensor, C, could be evaluated in terms of the martensite volume fraction,  $\xi$ , by the rule of mixtures, however, the assumption  $C = C_A = C_{M(a)}$ , where the subscripts A and  $M_{(a)}$  denote austenite and the  $a_{th}$ - martensite HPV, is adopted here for simplicity since first principal calculations show that the elastic properties of the B2 and B19' phases are similar [61].

The above volumetric/deviatoric decomposition of the elastic energy, which accounts for cubic symmetry [45], is essentially a tension/compression split introduced to prevent cracking in regions under compression and was initially proposed by [62] for elastic isotropy. In the literature, there are different options for the tension/compression split with some common split models for elastic isotropy discussed in [62,63] and their generalization to anisotropy in [64]. The degradation function g(c) links the crack

phase-field and the mechanical fields. Common choices for the degradation function may be found in [65,66]. The typically assumed quadratic function

$$g(c) = (1 - c)^2$$
, (20)

is adopted here.

Interaction energy. – The interaction energy is defined through its rate as in [56]<sup>1</sup>

$$\dot{\psi}_{int} = (\mathbf{C} : \boldsymbol{\varepsilon}^e) : \dot{\boldsymbol{\varepsilon}}^p - \boldsymbol{\sigma}_A : (1 - \xi) \sum_{l=1}^{N_A} {}_{A} \widehat{\boldsymbol{\varepsilon}}_p^{(l)} \dot{\boldsymbol{\gamma}}_A^{(l)}, \tag{21}$$

and

$$\mathbf{\sigma}_{A} = \mathbf{C} : \mathbf{\varepsilon}^{e} + \sum_{(\alpha)=1}^{N_{t}} \xi^{(\alpha)} \mathbf{C} : \left(\mathbf{I} - \mathbf{S}^{(\alpha)}\right) : \left(\widehat{\mathbf{\varepsilon}}_{t}^{(\alpha)} + \mathbf{\varepsilon}_{M_{(\alpha)}}^{p} - \mathbf{\varepsilon}_{A}^{p}\right), \tag{22a}$$

$$\mathbf{\sigma}_{M_{(\alpha)}} = \mathbf{\sigma}_{A} - \mathbf{C} : \left(\mathbf{I} - \mathbf{S}^{(\alpha)}\right) : \left(\widehat{\mathbf{\epsilon}}_{t}^{(\alpha)} + \mathbf{\epsilon}_{M_{(\alpha)}}^{p} - \mathbf{\epsilon}_{A}^{p}\right). \tag{22b}$$

 $\sigma_A$  and  $\sigma_{M_{(\alpha)}}$  stand for the average stress values in the austenite and the  $\alpha_{\rm th}$ -martensite HPV,  $S^{(\alpha)}$  stands for the Eshelby's tensor of the  $\alpha_{\rm th}$ -martensite HPV, which depends on the elastic constants and shape of the variant, and I is the fourth-order unit tensor.

Chemical energy.- The chemical energy reads as

$$\psi_{ch}\left(T,\xi^{(a)}\right) = c_v \left[ (T - T_0) - T \ln\left(\frac{T}{T_0}\right) \right] + \frac{\lambda}{T_T} (T - T_T)\xi,\tag{23}$$

where the specific heat,  $c_v$ , is assumed to be phase-independent, which is a common engineering assumption. The parameter  $T_T$  is the phase equilibrium temperature and  $\lambda$  is the latent heat of transformation at temperature  $T_T$ .

**Fracture energy.**— As standard in the phase-field modeling of fracture, the volumetric approximation of total fracture energy through a crack density functional  $\Gamma_c$  is adopted

$$\int_{\Gamma} G_c ds \approx \int_{O} G_c \Gamma_c(c, \nabla c) dx, \tag{24}$$

where the evolving internal discontinuity boundary,  $\Gamma$ , represents a set of discrete cracks,  $\mathcal{G}_c$  is the energy expended to create a unit area of fracture surface, and the damage-like, phase-field variable,  $0 \le c \le 1$ , approximates the fracture surfaces, taking the value 0 away from the crack and the value 1 within the crack, and, thus, the phase-field contribution on the free energy is postulated as

$$\psi_{\varepsilon_r}(c, \nabla c) = \mathcal{G}_{\varepsilon}\Gamma_{\varepsilon}(c, \nabla c). \tag{25}$$

The crack density functional is typically given as

$$\Gamma_c(c, \nabla c) = \frac{1}{w_0} \left[ \frac{1}{\ell} w(c) + 4\ell \left( \nabla c \cdot \nabla c \right) \right]; \quad w_0 = 8 \int_0^1 \sqrt{w(s)} ds, \tag{26}$$

where  $\ell > 0$  is a model length parameter that controls the width of the smooth approximation of the cracks,  $w(c) \in [0,1]$ , subject to the constraints w(0) = 0 and w(1) = 1, is a function that governs the shape of the regularized profile of the phase field, and  $w_0 > 0$  is a normalization constant. A quadratic function  $w(c) = c^2$  is most widely used, yielding

$$\Gamma_c(c, \nabla c) = \frac{1}{4\ell} \left( c^2 + 4\ell^2 \nabla c \cdot \nabla c \right). \tag{27}$$

Other choices have also been explored in literature [66-68].

## 3.3.2. Constitutive equations & dissipation inequality

The standard thermodynamical procedure, commonly referred to as the Coleman–Noll procedure, applied to the dissipation inequality

$$D = \mathbf{\sigma} : \mathbf{\hat{\epsilon}} - s\dot{T} + \mathbf{\hat{\zeta}} \cdot \nabla \dot{c} - \pi \dot{c} - \dot{\psi} = \left(\mathbf{\sigma} - g(c)\frac{\partial W_{el}^+}{\partial \mathbf{\hat{\epsilon}}^e} - \frac{\partial W_{el}^-}{\partial \mathbf{\hat{\epsilon}}^e}\right) : \mathbf{\hat{\epsilon}}^e + \left(s - c\ln\frac{T}{T_0} + \frac{\lambda}{T_0}\xi\right)\dot{T}$$

$$+ \sum_{\alpha=1}^{N_t} \left[\mathbf{\sigma} : \mathbf{\hat{\epsilon}}_t^{(\alpha)} - \frac{\lambda}{T_T}(T - T_T)\right] \dot{\xi}^{(\alpha)} + (1 - \xi)\mathbf{\sigma}_A : \sum_{l=1}^{N_A} A\mathbf{\hat{\epsilon}}_p^{(l)}\dot{\gamma}_A^{(l)}$$

$$+ \left(\mathbf{\hat{\zeta}} - \mathcal{G}_c \frac{\partial \Gamma_c}{\partial \mathbf{\nabla} c}\right) \cdot \mathbf{\nabla} \dot{c} - \left(\pi + g'(c)\mathbf{W}_{el}^+ + \mathcal{G}_c \frac{\partial \Gamma_c}{\partial c}\right) \dot{c} \ge 0, \tag{28}$$

<sup>&</sup>lt;sup>1</sup> The derivation of the interaction term in [56] is based on the Mori–Tanaka and Kröner micromechanical assumptions and the instantaneous growth hypothesis according to which the martensitic domains form instantaneously.

obtained via chain rule differentiation on the Helmholtz free energy with respect to its variables set, yields the constitutive relationships

$$\mathbf{\sigma} = g(c)\frac{\partial W_{el}^{+}}{\partial \mathbf{\varepsilon}^{e}} + \frac{\partial W_{el}^{-}}{\partial \mathbf{\varepsilon}^{e}}$$
(29)

$$s = c \ln \frac{T}{T_0} - \frac{\lambda}{T_0} \xi \tag{30}$$

$$\zeta = \mathcal{G}_c \frac{\partial \Gamma_c}{\partial \mathbf{\nabla} c} = 2\mathcal{G}_c \ell \mathbf{\nabla} c,\tag{31}$$

and the reduced dissipation expression

$$D = \sum_{\alpha=1}^{N_t} \left[ \mathbf{\sigma} : \hat{\mathbf{\epsilon}}_t^{(\alpha)} - \frac{\lambda}{T_T} (T - T_T) \right] \dot{\xi}^{(\alpha)} + (1 - \xi) \mathbf{\sigma}_A : \sum_{l=1}^{N_A} A \hat{\mathbf{\epsilon}}_p^{(l)} \dot{\gamma}_A^{(l)} - \left( \pi + g'(c) \mathbf{W}_{el}^+ + \mathcal{G}_c \frac{\partial \Gamma_c}{\partial c} \right) \dot{c} \ge 0.$$
 (32)

Assuming the material to be strongly dissipative, inequality (32) can be satisfied if

$$\begin{cases} D^{I} = \sum_{\alpha=1}^{N_{t}} \left[ \boldsymbol{\sigma} : \hat{\boldsymbol{\varepsilon}}_{t}^{(\alpha)} - \frac{\lambda}{T_{T}} (T - T_{T}) \right] \dot{\boldsymbol{\xi}}^{(\alpha)} > 0; & \exists \, \dot{\boldsymbol{\xi}}^{(\alpha)} \neq 0, \\ D^{p} = (1 - \boldsymbol{\xi}) \boldsymbol{\sigma}_{A} : \sum_{l=1}^{N_{A}} A \hat{\boldsymbol{\varepsilon}}_{p}^{(l)} \dot{\boldsymbol{\gamma}}_{A}^{(l)} > 0; & \exists \, \dot{\boldsymbol{\gamma}}_{A}^{(l)} > 0, \\ D^{c} = -\left( \pi + g'(c) W_{el}^{+} + G_{c} \frac{\partial \Gamma_{c}}{\partial c} \right) \dot{c} \geq 0; & \dot{c} > 0, \end{cases}$$

$$(33)$$

are enforced. It is assumed that these inequalities are obeyed at all times so that the dissipation inequality is concurrently satisfied.

## 3.3.3. Evolution equation for the phase-field parameter

The above dissipation inequality (33)c and possibly crack irreversibility, i.e.,  $\dot{c} \ge 0$ , are satisfied by assuming

$$\pi = -g'(c)\mathcal{H}^e - \mathcal{G}_c \frac{\partial \Gamma_c}{\partial c},\tag{34}$$

where the history functional,  $\mathcal{H}^e$ , introduced by [24], is subject to the Kuhn-Tucker conditions for loading and unloading

$$W_{sl}^{+} - H^{e} \le 0, \quad \dot{H}^{e} (W_{sl}^{+} - H^{e}) = 0,$$
 (35)

i.e., represents the maximum positive elastic energy obtained in a loading process.

In the above formulation, the evolution of the phase field variable, *i.e.*, the creation of new crack surfaces, is not recognized as a dissipative process since  $D^c \equiv 0$ . This is the case in general for rate-independent processes derived by the balance of a microforce. Given (10), (27) and (31), the phase-field evolution equation (34) reads

$$2\mathcal{G}_c \ell \, \nabla \cdot \nabla c = g'(c)\mathcal{H}^e + \frac{\mathcal{G}_c}{2\ell} c,\tag{36}$$

Note that the driving force for damage,  $-g'(c)\mathcal{H}^e$ , is assumed to be driven by the elastic energy in accordance with experimental observations suggesting that SMAs fracture in a stress-controlled manner, *i.e.*, phase transformation and plastic deformation are assumed to contribute in crack formation and growth indirectly through stress redistribution.

#### 3.3.4. Evolution equations for the internal state variables

From the above dissipation expressions, (33)a and b, the driving forces for phase transformation and plastic deformation can be invoked as the quasi-conservative thermodynamic forces conjugate to the respective internal variables. The evolution laws of martensitic transformation and plastic deformation are given as rate-dependent, power-law relations, in which the exponents are chosen sufficiently large to approximate rate-independent conditions [69].

**Martensitic transformation.**– For transformation of austenite to a particular martensite HPV, the driving force,  $F_{(\alpha)}^{t}$ , for this HPV should satisfy the following nonequilibrium condition

$$F_t^{(\alpha)} = \mathbf{\sigma} : \widehat{\mathbf{\epsilon}}_t^{(\alpha)} - \frac{\lambda}{T_T} (T - T_T) = {}_f f_t^{(\alpha)}, \tag{37}$$

where  $_f f_t^{(\alpha)} > 0$  is the HPV hardness, and  $\mathbf{\sigma} : \widehat{\mathbf{\epsilon}}_t^{(\alpha)}$  is the resolved stress on the  $\alpha_{\text{th}}$ -transformation system, but not in the classical Schmid sense since  $I^{(\alpha)}$  is typically not perpendicular to  $d^{(\alpha)}$ .

For this particular martensite HPV to transform back to austenite, the following condition must be met

$$-F_t^{(\alpha)} = -\mathbf{\sigma} : \hat{\mathbf{\epsilon}}_t^{(\alpha)} + \frac{\lambda}{T_T} (T - T_T) = {}_{r} f_t^{(\alpha)}, \tag{38}$$

where  $_r f_t^{(\alpha)} > 0$ .

The evolution law for the volume fraction of the  $\alpha_{th}$ -martensite HPV follows the power-law relation

$$\dot{\xi}^{(\alpha)} = \begin{cases} \dot{\xi}_0 \left( \frac{F_t^{(\alpha)}}{f_t^{(\alpha)}} \right)^n; & F_t^{(\alpha)} > 0, \text{ austenite} \to \text{martensite} \\ \\ -\dot{\xi}_0 \left( \frac{\left| F_t^{(\alpha)} \right|}{r f_t^{(\alpha)}} \right)^n; & F_t^{(\alpha)} < 0, \text{ martensite} \to \text{austenite} \end{cases}$$
(39)

where

$$\begin{cases} f f_t^{(\alpha)} = \sum_{(\beta)=1}^{N_t} H_t^{(\alpha)(\beta)} \xi^{(\beta)} + \xi^{(\alpha)} J_t \gamma + {}_f^c f_t^{(\alpha)}, \\ f_t^{(\alpha)} = \sum_{(\beta)=1}^{N_t} H_t^{(\alpha)(\beta)} \xi^{(\beta)} + \left(1 - \xi^{(\alpha)}\right) J_t \gamma + {}_f^c f_t^{(\alpha)}, \end{cases}$$

$$(40)$$

 $\dot{\xi}_0$  is a reference transformation strain rate,  $\left[H_t^{(\alpha)(\beta)}\right]$  is the interaction energy (constant) matrix between the different martensite HPVs, the scalar  $J_t > 0$  describes the transformation hardening due to plastic deformation,  $\gamma = \sum_{l=1}^{N_A} \left|\gamma_A^{(l)}\right|$  is the accumulated total slip, and  $c_f^c f_t^{(\alpha)}$ ,  $c_f^c f_t^{(\alpha)}$  are positive scalars.

**Plastic deformation of austenite.**– For plastic deformation of austenite, the driving force for dislocation slip of the  $l_{th}$ -slip system,  ${}_{A}F_{p}^{(l)}$ , should satisfy the following condition

$$\left|_{A}F_{p}^{(l)}\right| = \left|(1-\xi)\mathbf{\sigma}_{A}:_{A}\widehat{\mathbf{\varepsilon}}_{p}^{(l)}\right| = {}_{A}f_{p}^{(l)},\tag{41}$$

where  $_{A}f_{p}^{\left( l\right) }>0$  is the respective slip system hardness.

The slip rate in the  $l_{th}$ -slip system of austenite is given as

$$\dot{\gamma}_A^{(l)} = \dot{\gamma}_0 \left( \frac{{}_A F_p^{(l)}}{{}_A f_p^{(l)}} \right) \left( \frac{\left| {}_A F_p^{(l)} \right|}{{}_A f_p^{(l)}} \right)^{n-1}, \tag{42}$$

with the evolution law of the hardness,  $_{A}f_{p}^{(l)}$ , reading as

$${}_{A}\dot{f}_{p}^{(l)} = \sum_{r=1}^{N_{A}} {}_{A}H_{p}^{(l)(r)} \left| \dot{\gamma}_{A}^{(r)} \right|, \quad {}_{A}f_{p}^{(l)}(0) = {}_{A}^{c}f_{p}^{(l)}, \tag{43}$$

where  $\dot{\gamma}_0$  is reference plastic strain rate, the matrix

$${}_{A}H_{p}^{(l)(r)} = {}_{A}H_{p}\left[q^{(l)} + (1 - q^{(l)})\delta_{lr}\right] \left(1 - \frac{\gamma}{\gamma_{0}^{0}}\right)^{m_{p}},\tag{44}$$

describes the history-dependent rate of increase of the deformation resistance on slip system l due to shearing on slip system r, given in terms of the accumulated total slip,  $q^{(l)}$  stands for a constant latent-hardening parameter that ranges between 1 and 1.04, the positive scalar  $_AH_p$  is the initial slip-system hardening rate,  $m_p$  is the strain hardening exponent, and  $_A^cf_p^{(l)}$ ,  $_AH_p$ ,  $m_p$ ,  $\gamma_p^0$  are positive scalars.

# 3.3.5. Strong-form, boundary-value problem

In summary, the strong-form, boundary-value problem of the constitutive response reads as

Kinematics ((1), (2), (4), (7)). –

$$\begin{split} & \boldsymbol{\varepsilon} = \boldsymbol{\varepsilon}^e + \boldsymbol{\varepsilon}^t + \boldsymbol{\varepsilon}^p, \quad \boldsymbol{\varepsilon}^t = \sum_{\alpha=1}^{N_t} \widehat{\boldsymbol{\varepsilon}}_l^{(\alpha)} \boldsymbol{\xi}^{(\alpha)}, \quad \boldsymbol{\varepsilon}^p = (1-\xi) \boldsymbol{\varepsilon}_A^p + \sum_{\alpha=1}^{N_t} \boldsymbol{\xi}^{(\alpha)} \boldsymbol{\varepsilon}_{M_{(\alpha)}}^p, \\ & \hat{\boldsymbol{\varepsilon}}_A^p = \sum_{(\alpha)=1}^{N_t} \frac{\dot{\boldsymbol{\xi}}^{(\alpha)}}{1-\xi} \left( \boldsymbol{\varepsilon}_A^p - \boldsymbol{\varepsilon}_{M_{(\alpha)}}^p \right) + \sum_{l=1}^{N_A} A \widehat{\boldsymbol{\varepsilon}}_p^{(l)} \dot{\boldsymbol{\gamma}}_A^{(l)}, \quad \dot{\boldsymbol{\varepsilon}}_{M_{(\alpha)}}^p = \frac{\dot{\boldsymbol{\xi}}^{(\alpha)}}{\boldsymbol{\xi}^{(\alpha)}} \left( \boldsymbol{\varepsilon}_A^p - \boldsymbol{\varepsilon}_{M_{(\alpha)}}^p \right), \end{split}$$

where

$$\xi = \sum_{\alpha} \xi^{(\alpha)}.$$

Mechanical equilibrium (8). -

$$\nabla \cdot \mathbf{\sigma} + \mathbf{b} = 0.$$

Microforce balance ((36), (35), (17)). -

$$2\mathcal{G}_c \ell \nabla \cdot \nabla c = g'(c)\mathcal{H}^e + \frac{\mathcal{G}_c}{2\ell}c,$$

where  $\mathcal{H}^e$  is subject to

$$W_{el}^{+} - \mathcal{H}^{e} \leq 0, \quad \dot{\mathcal{H}}^{e} \geq 0, \quad \dot{\mathcal{H}}^{e} \left(W_{el}^{+} - \mathcal{H}^{e}\right) = 0,$$

and

$$W_{el}^{+} = \left(C_{11} + \frac{C_{12}}{6}\right) \left\langle \text{tr}(\mathbf{\epsilon}^{e})\right\rangle_{+}^{2} + C_{44} \left(\mathbf{\epsilon}_{dev}^{e} : \mathbf{\epsilon}_{dev}^{e}\right) + \left(\frac{C_{11} - C_{12}}{2} - C_{44}\right) \sum_{r=1}^{3} \left(\bar{\epsilon}_{dev,rr}^{e}\right)^{2},$$

Constitutive equation ((29), (18)). -

$$\mathbf{\sigma} = g(c) \frac{\partial \mathbf{W}_{el}^+}{\partial \mathbf{F}^e} + \frac{\partial \mathbf{W}_{el}^-}{\partial \mathbf{F}^e},$$

where

$$\mathbf{W}_{el}^{-} = \left(C_{11} + \frac{C_{12}}{6}\right) \langle \operatorname{tr}(\mathbf{\epsilon}^{e}) \rangle_{-}^{2}.$$

Evolution equations ((39), (37), (40), (42), (41), (43), (44), (22a)). -

$$\dot{\xi}^{(\alpha)} = \begin{cases} \dot{\xi}_0 \left( \frac{F_t^{(\alpha)}}{f_t^{(\alpha)}} \right)^n; & F_t^{(\alpha)} > 0, \text{ austenite} \rightarrow \text{martensite}, \\ \\ -\dot{\xi}_0 \left( \frac{\left| F_t^{(\alpha)} \right|}{f_t^{f_t^{(\alpha)}}} \right)^n; & F_t^{(\alpha)} < 0, \text{ martensite} \rightarrow \text{austenite}, \end{cases}$$

where

$$F_{t}^{(\alpha)} = \mathbf{\sigma} : \hat{\mathbf{\epsilon}}_{t}^{(\alpha)} - \frac{\lambda}{T_{T}} (T - T_{T}), \begin{cases} \int_{t}^{f} f_{t}^{(\alpha)} = \sum_{(\beta)=1}^{N_{t}} H_{t}^{(\alpha)(\beta)} \xi^{(\beta)} + \xi^{(\alpha)} J_{t} \gamma + {}_{f}^{c} f_{t}^{(\alpha)} \\ \int_{t}^{N_{t}} \int_{t}^{f} f_{t}^{(\alpha)} = \sum_{(\beta)=1}^{N_{t}} H_{t}^{(\alpha)(\beta)} \xi^{(\beta)} + \left(1 - \xi^{(\alpha)}\right) J_{t} \gamma + {}_{r}^{c} f_{t}^{(\alpha)} \end{cases}, \quad \gamma = \sum_{l=1}^{N_{A}} \left| \gamma_{A}^{(l)} \right|,$$

and

$$\dot{\gamma}_A^{(l)} = \dot{\gamma}_0 \left( \frac{{}_A F_p^{(l)}}{{}_A f_p^{(l)}} \right) \left( \frac{\left| {}_A F_p^{(l)} \right|}{{}_A f_p^{(l)}} \right)^{n-1},$$

where

$${}_{A}F_{p}^{(l)} = (1-\xi)\mathbf{\sigma}_{A} \, : \, {}_{A}\widehat{\mathbf{\epsilon}}_{p}^{(l)}, \quad \begin{cases} {}_{A}\dot{f}_{p}^{(l)} = \sum_{r=1}^{N_{A}} {}_{A}H_{p}^{(l)(r)} \left| \dot{\gamma}_{A}^{(r)} \right|, \quad {}_{A}H_{p}^{(l)(r)} = {}_{A}H_{p} \left[ q^{(l)} + (1-q^{(l)})\delta_{lr} \right] \left( 1 - \frac{\gamma}{\gamma_{p}^{0}} \right)^{m_{p}}.$$

$$\sigma_A = \mathbf{C} \, : \, \mathbf{\varepsilon}^e + \sum_{(\alpha)=1}^{N_t} \, \xi^{(\alpha)} \mathbf{C} \, : \, \left( \mathbf{I} - \mathbf{S}^{(\alpha)} \right) \, : \, \left( \widehat{\mathbf{\varepsilon}}_t^{(\alpha)} + \mathbf{\varepsilon}_{M_{(\alpha)}}^p - \mathbf{\varepsilon}_A^p \right).$$

Boundary conditions. - The equilibrium equations are subject to the boundary conditions

$$\begin{cases} u \Big|_{\partial Q^{u}} = \bar{u}, \\ \mathbf{\sigma} \cdot \mathbf{n} \Big|_{\partial Q^{t}} = \bar{t}, \\ \mathbf{\nabla} c \cdot \mathbf{n} \Big|_{\partial Q} = 0, \end{cases}$$

$$(45)$$

where  $\underline{\bar{u}}$  and  $\underline{\bar{t}}$  are prescribed displacement and tractions on the Dirichlet,  $\partial Q^u$ , and von Neumann,  $\partial Q^t$ , boundaries, respectively  $(\partial Q = \overline{\partial Q^u} \cup \partial Q^t)$  and  $\emptyset = \partial Q^u \cap \partial Q^t)$ .

# 4. Algorithmic implementation

The variational form of the boundary-value problem given above reads as:

Given **b** and  $\bar{\mathbf{t}}$ , find  $(\mathbf{u}, c) \in \mathcal{V}_{\mathbf{u}} \times H^1(\mathcal{Q}_t)$ , such that

$$\begin{cases}
\int_{Q} \left[ \mathbf{\sigma} : \nabla \mathbf{v} - \mathbf{b} \cdot \mathbf{v} \right] d\mathbf{x} - \int_{\partial Q} \mathbf{\bar{t}} \cdot \mathbf{v} \, ds = 0, \\
\int_{Q} \left[ 2G_{c} \ell \, \nabla c \cdot \nabla w + g'(c) \mathcal{H}^{e} w + \frac{G_{c}}{2\ell} cw \right] d\mathbf{x} = 0,
\end{cases} \tag{46}$$

for all  $(v, w) \in \mathcal{V}^0_{\cdot \cdot \cdot} \times H^1(\mathcal{Q})$ , where

$$\mathcal{V}_{u} = \left\{ \mathbf{u} \in H^{1}(\mathcal{Q}); \mathbf{u} \Big|_{\partial \mathcal{O}^{u}} = \bar{\mathbf{u}} \right\}, \quad \mathcal{V}_{u}^{0} = \left\{ \mathbf{u} \in H^{1}(\mathcal{Q}); \mathbf{u} \Big|_{\partial \mathcal{O}^{u}} = 0 \right\}. \tag{47}$$

Due to the non-convexity of the free energy  $\psi$  in both the unknown fields u and c, conventional monolithic solvers of the above system suffer from associated iterative convergence issues. A line search solver [70], a modified Newton-Raphson method [71], quasi-Newton methods [72–74] and an arc-length method based on fracture energy [75] have been proposed, among others, to circumvent the convergence issues. Staggered solution schemes take advantage of the convexity of  $\psi$  in each argument separately to algorithmically decouple the governing equations by keeping one field frozen while solving for the other. Staggered schemes are robust but computationally demanding often requiring small time steps and large number of iterations for convergence [24,26].

Here, following the Galerkin method and a usual finite-element approximation of the functional spaces of the weak form, the discretized version of the above system of equations is solved by a single-pass staggered scheme [24] as follows.

Given the converged values  $\left\{ \boldsymbol{u}_t, c_t, \mathcal{H}_t^e, \xi_t^\alpha, \left(\gamma_A^l\right)_t \right\}$  at a time t and the predefined temperature value at  $t + \Delta t$ ,  $T_{t+\Delta t}$ , where the value of a quantity  $\alpha$  at time t is denoted as  $\alpha_t$  and the increment in  $\alpha$  over a time interval  $\Delta t$  as  $\Delta \alpha = \alpha_{t+\Delta t} - \alpha_t$ :

- Compute  $c_{t+At}$  from the microforce balance equation (46)b using  $\mathcal{H}_t^e$ .
- Compute  $u_{t+\Delta t}$  from the linearized mechanical equilibrium equation (46)a

$$\int_{O} \mathbf{\sigma} : \nabla v dx + \int_{O} \nabla \left( \Delta u^{i} \right) : \frac{\partial \mathbf{\sigma}}{\partial \nabla u^{i}} : \nabla v dx - \int_{O} \mathbf{b} \cdot v dx - \int_{\partial O} \bar{\mathbf{t}} \cdot v \, ds = 0, \tag{48}$$

using the Newton–Raphson method, which results in a global loop of displacement incrementation, where  $u^i$  stands for the displacement at iteration i and  $\Delta u^i$  is the unknown increment to be solved for. At every iteration during this loop, compute the stress value  $\sigma\left(u^i,c_{t+\Delta t},\xi^{\alpha}_{t+\Delta t},\left(\gamma^l_A\right)_{t+\Delta t},T_{t+\Delta t}\right)$  by the change in martensite volume fractions,  $\Delta \xi^{\alpha}$  and shear rates,  $\Delta \gamma^l_A$ , through an explicit numerical integration method, which results in a tangent stiffness expression considerably reduced from the elastic stiffness; in explicit integration, the maximum allowable time step is inversely related to the relevant material stiffness [76,77].  $\Delta \xi^{\alpha}$  and  $\Delta \gamma^l_A$  are computed by the system of equations

$$\begin{cases}
\Delta \xi^{\alpha} = \dot{\xi}_{t}^{\alpha} \left[ 1 + \theta n \left( \frac{\Delta F_{t}^{\alpha}}{F_{t}^{\alpha}} - \frac{\Delta f_{t}^{\alpha}}{f_{t}^{\alpha}} \right) \right] \Delta t, \\
\Delta \gamma_{A}^{l} = \left( \dot{\gamma}_{A}^{l} \right)_{t} \left[ 1 + \theta n \left( \frac{\Delta_{A} F_{p}^{l}}{A F_{p}^{l}} - \frac{\Delta_{A} f_{p}^{l}}{A f_{p}^{l}} \right) \right] \Delta t,
\end{cases} \tag{49}$$

where the parameter  $\theta$  ranges from 0 to 1, which is consistent, *i.e.*, can be solved for small time steps. The above system of equations results by linear interpolation within  $\Delta t$ 

$$\begin{cases}
\Delta \xi^{\alpha} = \left[ (1 - \theta) \dot{\xi}_{t}^{\alpha} + \theta \dot{\xi}_{t+\Delta t}^{\alpha} \right] \Delta t, \\
\Delta \gamma_{A}^{l} = \left[ (1 - \theta) \left( \dot{\gamma}_{A}^{l} \right)_{t} + \theta \left( \dot{\gamma}_{A}^{l} \right)_{t+\Delta t} \right] \Delta t,
\end{cases} \tag{50}$$

and replacing  $\dot{\xi}^{\alpha}_{t+\Delta t}$  and  $\left(\dot{\gamma}^{l}_{A}\right)_{t+\Delta t}$  with their Taylor expansion

$$\begin{cases} \dot{\xi}_{t+\Delta t}^{\alpha} = \dot{\xi}_{t}^{\alpha} + \frac{\partial \dot{\xi}_{t}^{\alpha}}{\partial F_{t}^{\alpha}} \bigg|_{t} \Delta F_{t}^{\alpha} + \frac{\partial \dot{\xi}_{t}^{\alpha}}{\partial f_{t}^{\alpha}} \bigg|_{t} \Delta f_{t}^{\alpha}, \\ (\dot{\gamma}_{A}^{l})_{t+\Delta t} = (\dot{\gamma}_{A}^{l})_{t} + \frac{\partial \left(\dot{\gamma}_{A}^{l}\right)_{t}}{\partial_{A} F_{p}^{l}} \bigg|_{t} \Delta_{A} F_{p}^{l} + \frac{\partial \left(\dot{\gamma}_{A}^{l}\right)_{t}}{\partial_{A} f_{p}^{l}} \bigg|_{t} \Delta_{A} f_{p}^{l}, \end{cases}$$

which in view of the evolution equations read as

$$\begin{cases} \dot{\xi}_{t+\Delta t}^{\alpha} = \dot{\xi}_{t}^{\alpha} \left[ 1 + n \left( \frac{\Delta F_{t}^{\alpha}}{F_{t}^{\alpha}} - \frac{\Delta f_{t}^{\alpha}}{f_{t}^{\alpha}} \right) \right], \\ (\dot{\gamma}_{A}^{l})_{t+\Delta t} = (\dot{\gamma}_{A}^{l})_{t} \left[ 1 + n \left( \frac{\Delta_{A} F_{p}^{l}}{A F_{p}^{l}} - \frac{\Delta_{A} f_{p}^{l}}{A f_{p}^{l}} \right) \right]. \end{cases}$$

$$(51)$$

· Determine the history variable

$$\mathcal{H}_{t+\Delta t}^{e} = \begin{cases} W_{el}^{+} \left( \mathbf{u}_{t+\Delta t}, c_{t+\Delta t}, \xi_{t+\Delta t}^{\alpha}, \left( \gamma_{A}^{l} \right)_{t+\Delta t} \right), & W_{el}^{+} \left( \mathbf{u}_{t+\Delta t}, c_{t+\Delta t}, \xi_{t+\Delta t}^{\alpha}, \left( \gamma_{A}^{l} \right)_{t+\Delta t} \right) > \mathcal{H}_{t}^{e}, \\ \mathcal{H}_{t}^{e}, & \text{otherwise.} \end{cases}$$

The above algorithm is implemented in ABAQUS suite via a UMAT and a HETVAL subroutines [78]. The above implementation is conditionally stable and requires the time increments employed to be sufficiently small.

#### 5. Numerical examples

The material parameter values in the numerical simulations presented below are listed in Table 1 [55]. The transformation and slip parameters were determined from the experiments of Gall et al. [79] on Ni<sub>50.9</sub>Ti (at.%). Of the 192 possible HPVs predicted by the crystallographic theory of martensite only the 24 Type II-1 HPVs frequently observed in experiments are considered. The components of the vectors  $l^{\alpha}$  and  $d^{\alpha}$  are given in [80,81] and  $g_t = 0.1308$ . The interaction matrix  $H_t^{(\alpha)(\beta)}$ , given in [82], is not accounted for since simulations showed that its inclusion overestimates the strain hardening observed in the experimental data. The "viscous" parameter n is set to a high value, n = 50, to approximate the rate-independent response of NiTi. The initial critical forces for forward phase transformation are assumed identical for all martensite HPVs,  $_{f}^{c}f_{t}^{\alpha}=_{f}^{c}f_{t}$ , and, similarly  $_{r}^{c}f_{t}^{\alpha}=_{r}^{c}f_{t}$  and  $H_{t}^{\alpha}=H_{t}$ . Experimentally, only slip in the system families (100) (001), (100) (011), (110) (111) has been observed [52], and, thus, only these slip families are included in the simulations. The initial critical forces for slip in these systems,  ${}^{c}_{A}f^{l}_{p}$ , are assumed identical for each family, and are thus reduced to  ${}_A^c f_p^r$  (r=1,2,3). Note that  $\gamma_p^0$  and  $m_p$  in (17) cannot be reliably calibrated from the experiments reported in [79] and are thus assumed null. The reference transformation rate value,  $\dot{\xi}_0$ , and the reference plastic strain rate,  $\dot{\gamma}_0$ , are representative of the applied loading rate [83]. The Eshelby tensor is assumed identical for all HPVs and corresponds to oblate spheroids - the martensite phase is formed as thin platelets, needles, or laths within the austenite parent phase - in an isotropic matrix obtained by the isotropization of the stiffness tensor,  $\mathbf{C}^{iso} \equiv (\mathbf{C} :: \mathbf{I}_V) \mathbf{I}_V + \frac{1}{5} (\mathbf{C} :: \mathbf{I}_D) \mathbf{I}_D$ , where  $\mathbf{I}_V = \frac{1}{2} \delta \otimes \delta$ and  $\mathbf{I}_D = \mathbf{I}_s - \mathbf{I}_V$  are the volumetric and deviatoric projection tensors, respectively,  $\mathbf{I}_s$  designates the fourth-order tensor with components  $I_{ijkl}^s = \frac{1}{2} \left( \delta_{ik} \delta_{jl} + \delta_{il} \delta_{jk} \right)$ , and  $\mathbf{A} :: \mathbf{B} = A_{ijkl} B_{lkji}$  for any fourth order tensors  $\mathbf{A}$  and  $\mathbf{B}$ . The lengths of the semi-axes of the ellipsoidal HPV inclusions are set as  $a_1 = a_2 = a$ ,  $a_3 = a/b$ , for b > 1. In the simulations, b is assumed equal to 4. The fracture toughness is reported in [5,50] while the length scale parameter ℓ is selected with consideration of the ultimate tensile strength of the material [24,25]. A scaled fracture toughness  $G_c^s = G_c/[1 + h_d/(4\ell)]$ , where  $h_d$  is the minimum mesh size  $(h_d = \sqrt{A})$  (or  $\sqrt[3]{A}$ ) is the area (or volume) of an element is used in the simulations as discussed in [84]. Finally, the meshes were generated so as to ensure that  $h_d < \ell/3$ .

## 5.1. Single-crystal specimen: Mechanical fracture

#### 5.1.1. Single-notched specimen

The single-notched specimen shown in Fig. 1 is considered first. A notch runs in the middle of the specimen up to the center of it. The upper surface of the specimen is set to be displaced by a distance  $u_b=3.3$  mm with a strain rate equal to  $4\cdot 10^{-4}$  at temperature T=275 K while both vertical and horizontal displacements are restricted on the bottom edge as depicted in the figure. The dimensionless load parameter  $\bar{u}$  stands for the ratio  $u(t)/u_b$ . Plane-strain conditions are imposed by preventing displacements in the through-thickness direction, thus, while the elements (6320 C3D8RT and C3D6T) and the formulation are 3D, the problem is effectively 2D.

The influence of the crystallographic orientation is investigated by performing simulations under loading in the [110], [111], and [221] directions. The crystallographic direction alters the elastic, phase transformation, and plastic deformation response resulting in different reaction force,  $F_{react}$ , vs load parameter,  $\bar{u}$ , curves (Fig. 1). In all simulations there is a stable crack growth regime due to irrecoverable strains left in the wake of the growing crack that provide crack shielding followed by abrupt rupture. Convergence of the solution during abrupt rupture is problematic. An initial drop in the load associated with the first instance of crack growth is observed in all cases. The distribution of martensite volume fraction,  $\xi$ , and the accumulated plastic strain,  $\bar{\epsilon}_p = \sqrt{\frac{3}{2}} \epsilon_{ij}^p \epsilon_{ij}^p$ , are depicted in Fig. 2 and the phase field parameter, c, in Fig. 3. Large transformation and plastic deformation zones of crystallographically dependent shapes are observed. Note that in all simulations the crack path is the mode I predicted path. Such a response is considered acceptable given (i) the cubic material symmetry (in terms of its elastic response) [23], (ii) the loading symmetry, which is sufficiently preserved by a nearly symmetric phase transformation zone (attributed to the large number of HPVs that form, more than 12 HPVs in all cases), and (iii) the experimental observation of a crack growing in the mode I predicted path in one of the two fracture experiments presented in [21].

## 5.1.2. Asymmetrically double-notched specimen

An asymmetrically double-notched plane strain specimen is investigated next to model mixed-mode fracture under different loading directions. The geometry is depicted in Fig. 4. In the simulations performed, the boundary conditions, strain rate, and temperature are the ones described in the previous section (Section 5.1.1) with the only difference that the specimen's upper surface displacement is set to  $u_b = 6.6$  mm. The domain is discretized using 25655 C3D8RT and C3D6T elements.

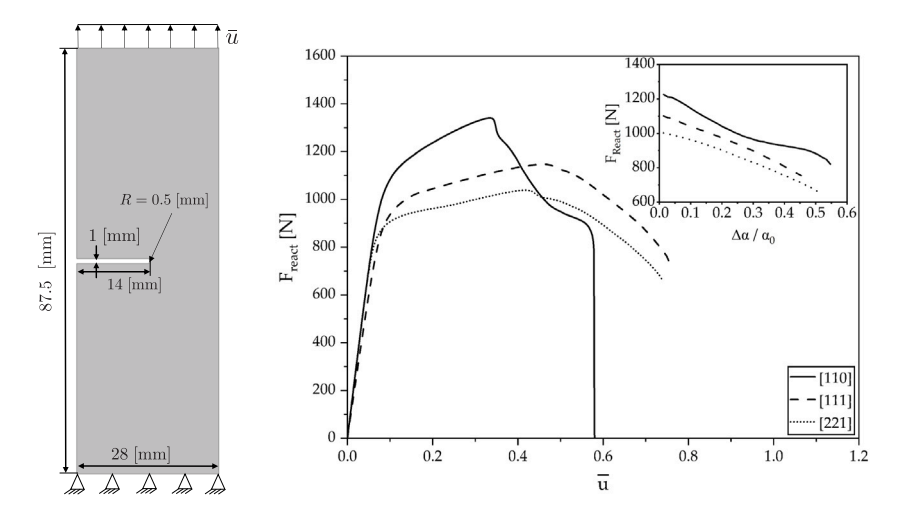


Fig. 1. Geometry, boundary conditions, and loading for the fracture of the single-notched single crystal NiTi specimen. The reaction force on the upper surface,  $F_{\rm react}$ , vs the load parameter,  $\bar{u}$ , curves for loading along three crystallographic direction, i.e., [110], [111], and [221], are also indicated and in the inset figure the  $F_{\rm react}$  vs  $\Delta a/a_0$  curves, where  $\Delta a/a_0$  stands for the ratio of the change in crack length,  $\Delta a$ , over the initial crack length,  $a_0$ .

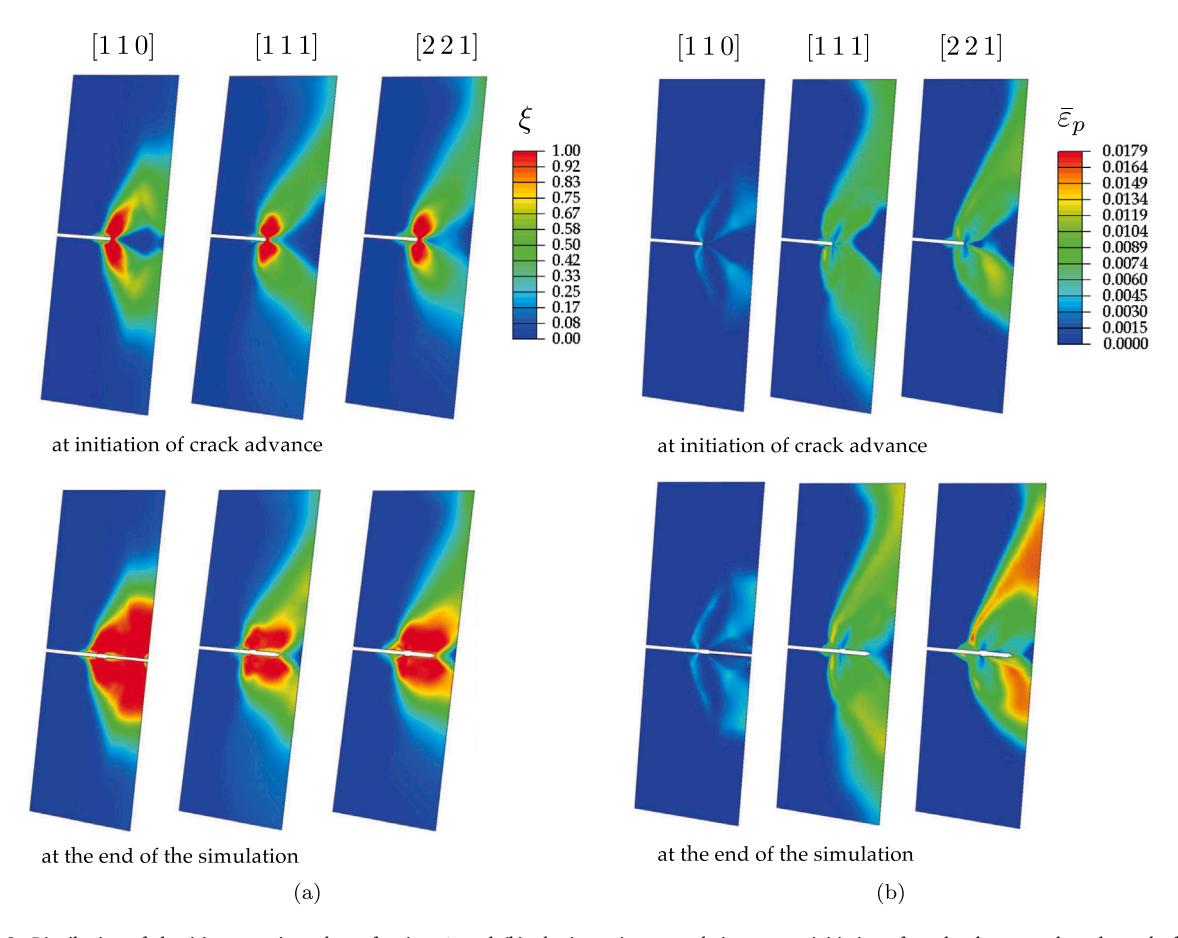


Fig. 2. Distribution of the (a) martensite volume fraction,  $\xi$ , and (b) plastic strain accumulation,  $\bar{\epsilon}_p$ , at initiation of crack advance and at the end of the simulations.

**Table 1** Model parameter values. The crystallographic data for the 24 martensite HPVs in NiTi is given in [80,81] and  $g_n = 0.1308$ . The strain rate exponent n is set to a high value, n = 50.

	parameter	value
	specific heat $c_v$ [MJ/(m <sup>3</sup> K)]	2.1
Austenite	elastic constant $C_{11}^A$ [GPa]	130
	elastic constant $C_{12}^{A}$ [GPa]	98
	elastic constant $C_{44}^{A}$ [GPa]	34
HPVs	elastic constants $\overrightarrow{\mathbf{C}}_{M_{(a)}} = \mathbf{C}_A$	

(b) Transformation	Parameters
--------------------	------------

parameter	value
equilibrium transformation temperature, $T_T$ , [K]	257
latent heat of transformation per unit volume, $\lambda$ , [MJ/m <sup>3</sup> ]	154
critical force for forward phase transformation, $_{t}^{c}f_{t}$ , [MPa]	2
critical force for reverse phase transformation, [f], [MPa]	20
hardening coefficient, $J_{i}$ ,[MPa]	50

#### (c) Austenite Plastic Deformation Parameters

parameter	value
critical force for slip in $\langle 100 \rangle \{001\}$ , ${}^c_A f^1_p$ , [MPa]	700
critical force for slip in $\langle 100 \rangle \{011\}$ , $_A^c f_p^2$ , [MPa]	550
critical force for slip in $\langle 110 \rangle \{\bar{1}11\}, {}^{c}_{A}f^{3}_{p}, [MPa]$	500
hardening coefficient, $_{A}H_{_{p}}$ , [MPa]	40
ratio of self to latent hardening, $q$	1.4

## (d) Phase-field parameters

parameter	value
ℓ [mm]	0.725
$G_c$ [MPa.mm]	150

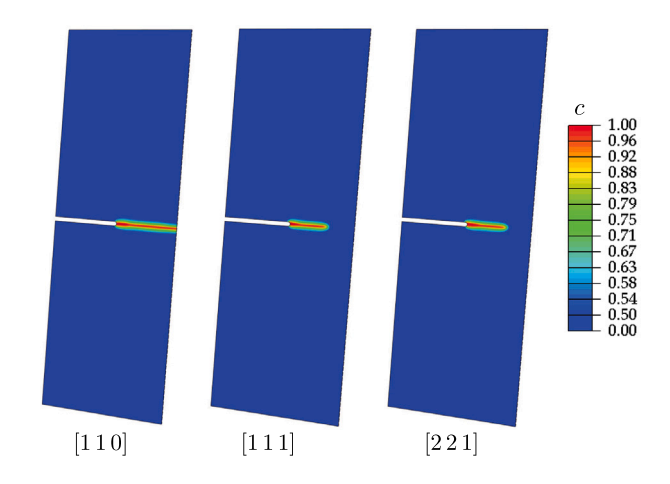


Fig. 3. The distribution of the phase-field parameter, c, at the end of the simulations.

The martensite volume fraction,  $\xi$ , accumulated plastic strain,  $\bar{\epsilon}_p$ , and the phase field parameter, c, distributions are shown in Figs. 5 and 6. Similarly to the single-notched specimen, the shapes of the transformation and plastic deformation zones are crystallographically dependent. In all simulations, the failure of the specimen is due to cracks extending from the notches towards each other, initially in a stable manner before abrupt rupture takes place. An initial drop in the load associated with the first instance of crack growth is observed in all cases. Contrary to the single-notched specimen, crystallographic directions do have an impact on the crack path; it is conjectured that the effect of crystallography in the driving force for crack advance is augmented by the mixed-mode of fracture. The ability to naturally predict the path of the two distinct cracks is a significant advantage of the phase-field approach over other fracture modeling approaches that require explicit crack tracking algorithms.

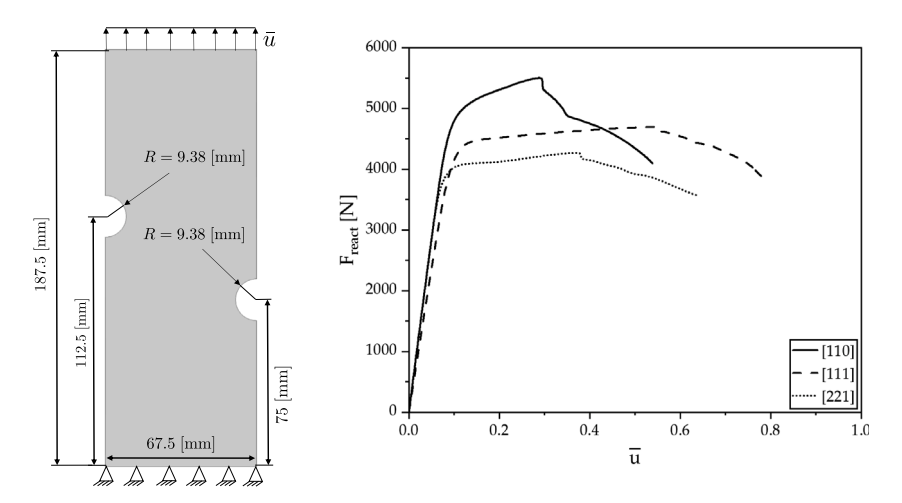


Fig. 4. Geometry, boundary conditions, and loading for the fracture of the asymmetrically double-notched single crystal NiTi specimen. The reaction force on the upper surface,  $F_{react}$ , vs the load parameter,  $\bar{u}$ , curves for loading along three crystallographic direction, i.e., [110], [111], and [221], are also indicated.

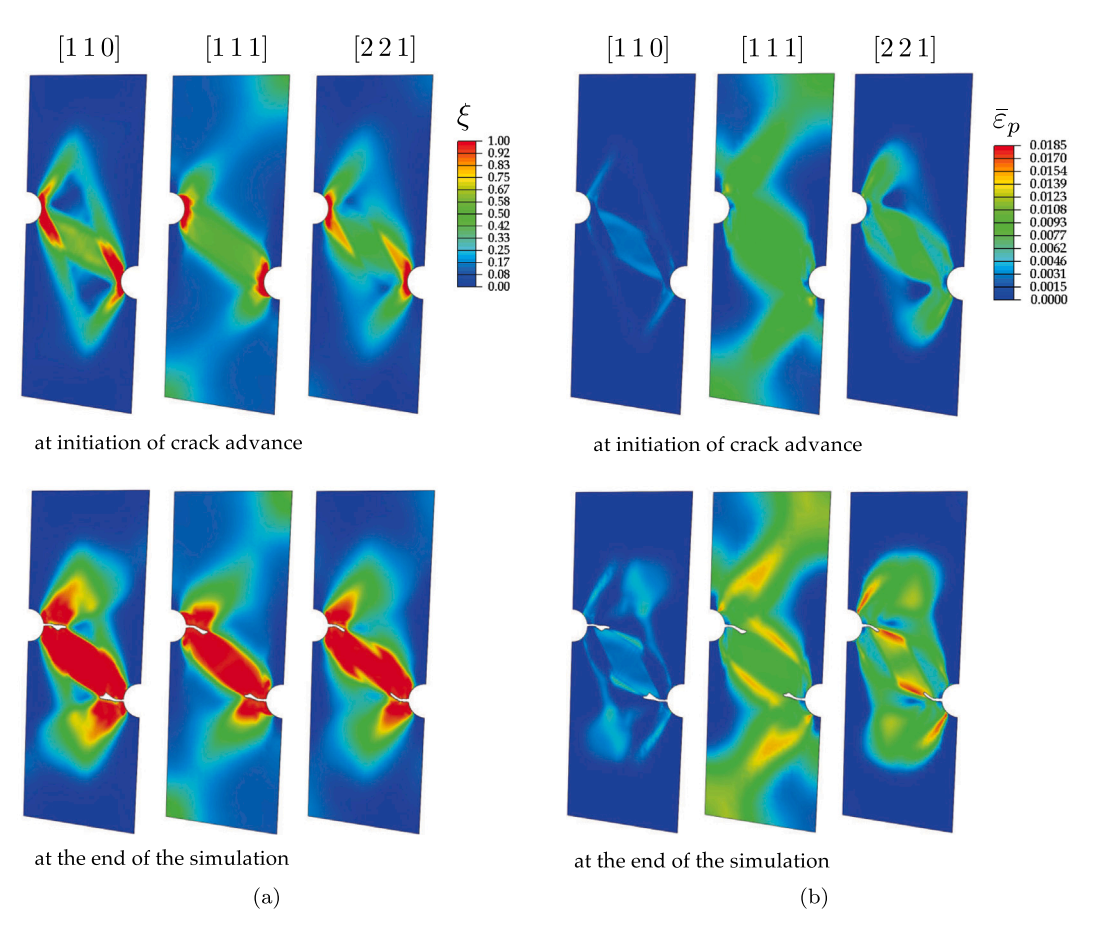


Fig. 5. Distribution of the (a) martensite volume fraction,  $\xi$ , and (b) plastic strain accumulation,  $\bar{\epsilon}_p$ , at initiation of crack advance and at the end of the simulations.

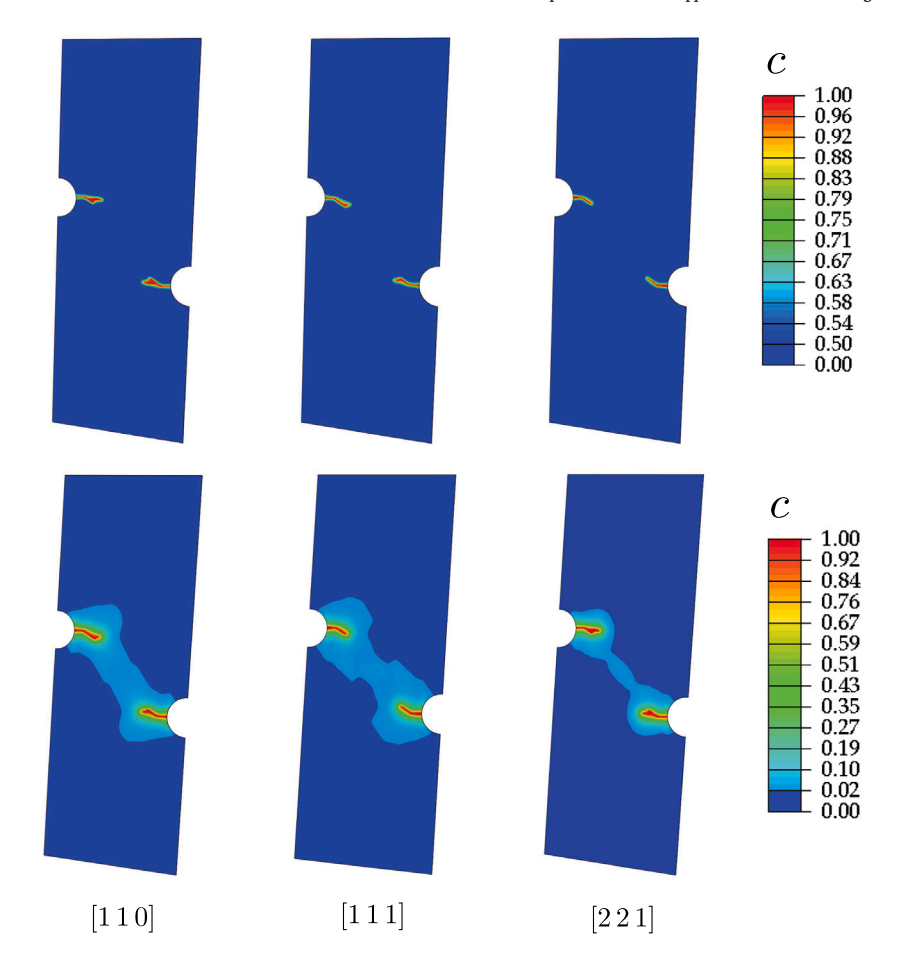


Fig. 6. The distribution of the phase-field parameter, c, at the end of the simulations. Please, note that for visualization purposes the distributions are presented both for (up) c > 0.5 and (down) c > 0.

## 5.2. Polycrystalline specimen: Thermomechanical fracture

The simulations presented in this section are for the single-notched geometry depicted in Fig. 7 but for a polycrystalline material. The domain consists of 501 grains of random orientation and size and is discretized into 41973 C3D8RT and C3D6T elements. The grains are created by Voronoi tessellation in Neper and the discretization is performed in BETA CAE. Two simulations are performed:

- Simulation *M.* the boundary conditions, strain rate, and temperature used are the ones described in Section 5.1.1, resulting in isothermal mechanical fracture.
- Simulation TM.— the upper surface of the specimen is first loaded to 1023 N, which corresponds to approximately 176 MPa stress, at temperature T=275 K, with a load rate equal to 2.33 N/s while both vertical and horizontal displacements are restricted on the bottom edge and then the specimen is cooled with a temperature rate -0.4375 K/s while the bias load is kept fixed; such loading path can utilize SMAs as actuators and results in thermomechanical fracture.

The martensite volume fraction,  $\xi$ , accumulated plastic strain,  $\bar{\epsilon}_p$ , and the phase field parameter, c, distributions at the end of Simulation M are shown in Fig. 8. The effect of the crystallographic direction of the grains in the  $\xi$  and  $\bar{\epsilon}_p$  distributions is evident. The crack travels through the grains, changing its direction as it propagates due to texture, while it remains nearly perpendicular to the applied load, as depicted in Fig. 9.

In Fig. 10, the martensite volume fraction,  $\xi$ , and effective plastic strain  $\bar{\varepsilon}_p$ , evolution and crack growth pattern at the end of mechanical loading and at the end of the simulation are shown for Simulation TM. Mechanical loading alone was not sufficient to induced crack advance. Cooling, however, resulted in a large-scale phase transformation and an associated stress redistribution sufficient to promote crack advance, leading to an unstable crack growth at  $T \approx 247$  K. Such a thermomechanical fracture has been observed experimentally in double-notched NiTi specimen [85] and discussed in [86]. The crack path is again nearly perpendicular to the load direction while changing its direction as it travels through the grains.

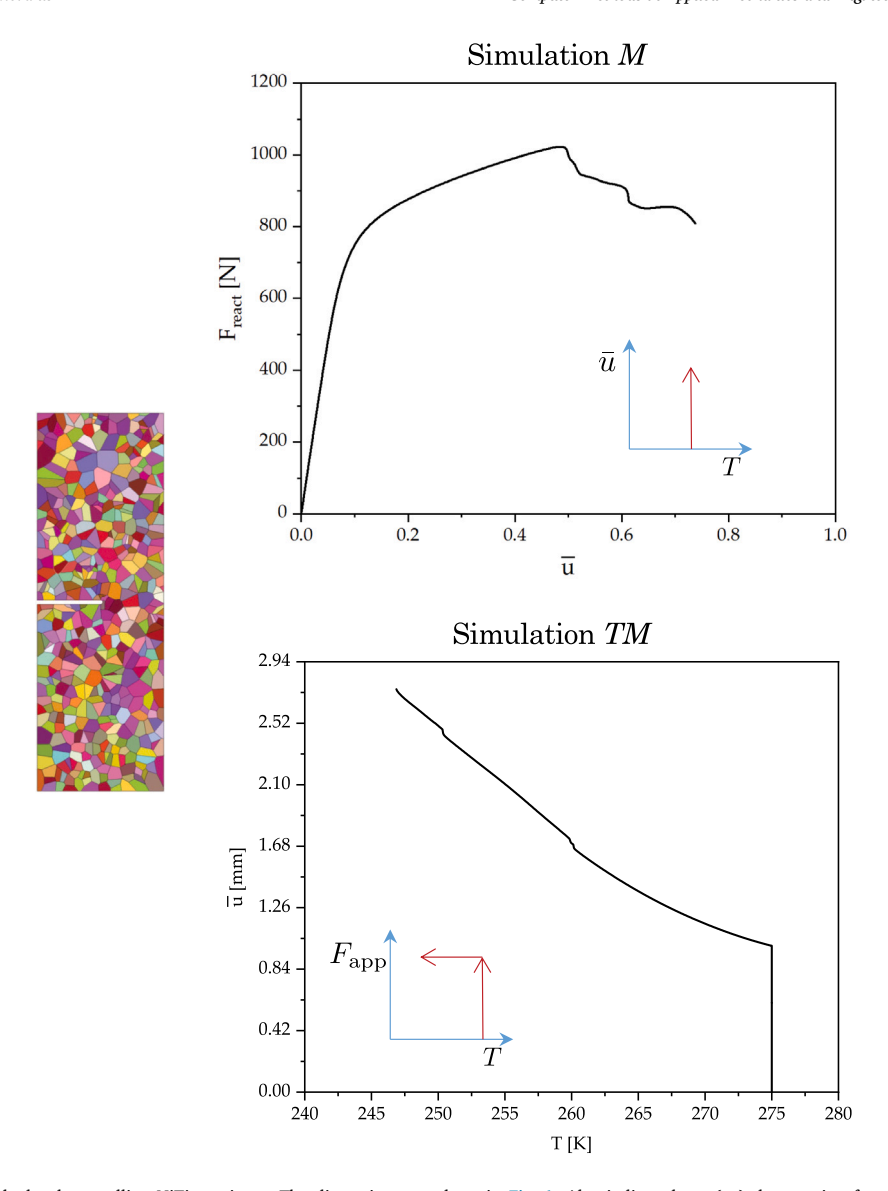


Fig. 7. The single-notched polycrystalline NiTi specimen. The dimensions are those in Fig. 1. Also indicated are (up) the reaction force on the upper surface,  $F_{\text{react}}$ , vs the load parameter,  $\bar{u}$ , curve for Simulation M with the corresponding loading conditions shown in the inset and (up) the displacement on the upper surface,  $\bar{u} = u/u_M$ , vs temperature, T, curve, where  $u_M$  is the displacement at the end of mechanical loading, for Simulation TM with the corresponding loading conditions shown in the inset.

## 6. Conclusions

A phase-field model for thermomechanically-induced fracture in single crystal NiTi is proposed under the small strain assumption. The model accounts for reversible phase transformation from austenite to martensite HPVs and plastic deformation in the austenite phase. Interactions between transformation and plastic deformation are accounted for by a mean-field micromechanics evaluation of the internal stress raise due to deformation incompatibility at the austenite–martensite interfaces, which results in transformation-induced plastic deformation. Based on experimental observations that indicate NiTi fracture as stress-driven, only the elastic strain energy is assumed to contribute to the driving force for crack formation and growth, *i.e.*, inelastic deformation is assumed to have a negligible contribution to the evolution of the intrinsic damage mechanisms at the fracture process zone. The algorithmic implementation is based on viscous regularizations of the phase transformation and plastic deformation treatments, *i.e.*, all HPVs and slip systems are active at all times, an explicit numerical integration, which results in a tangent stiffness expression considerably reduced from the elastic stiffness, and a staggered solution scheme, which algorithmically decouples the governing equations. The model is restricted to quasistatic mechanical loading, thermal loading sufficiently slow with respect to the time rate of heat transfer by conduction, and a temperature range in which stress-induced martensitic transformation is not suppressed. The model

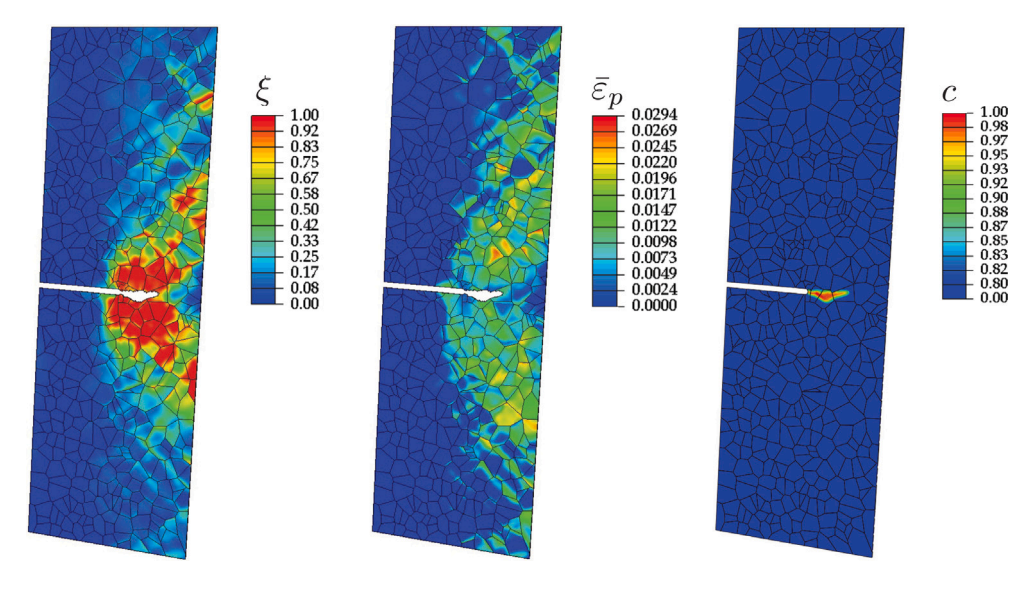


Fig. 8. Distribution of the martensite volume fraction,  $\xi$ , plastic strain accumulation,  $\bar{\epsilon}_p$ , and phase-field parameter, c, at the end of Simulation M.

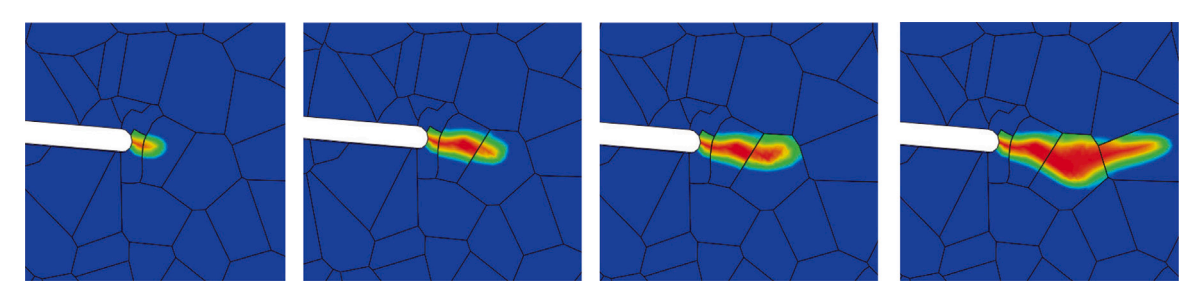


Fig. 9. Evolution of crack advance at different loading instances of Simulation M.

is shown able to capture transformation-induced toughening, *i.e.*, stable crack advance attributed to the shielding effect of inelastic deformation left in the wake of the growing crack under nominal isothermal loading, actuation-induced fracture under a constant bias load, and crystallographic dependence on crack pattern.

#### CRediT authorship contribution statement

**D. Kavvadias:** Data curation, Formal analysis, Investigation, Validation, Visualization, Writing – original draft. **Th. Baxevanis:** Conceptualization, Formal analysis, Supervision, Writing – original draft, Writing – review & editing.

#### Declaration of competing interest

The authors declare the following financial interests/personal relationships which may be considered as potential competing interests: Theocharis Baxevanis reports financial support was provided by National Science Foundation.

## Data availability

Data will be made available on request.

# Acknowledgments

This study was supported by the National Science Foundation, United States under Grant no. CMMI-1917441. The authors acknowledge the ResearchComputingDataCore(RCDC) at the University of Houston for the supercomputing resources made available for conducting the research reported in this paper and BETA CAE for allowing us to use their software.

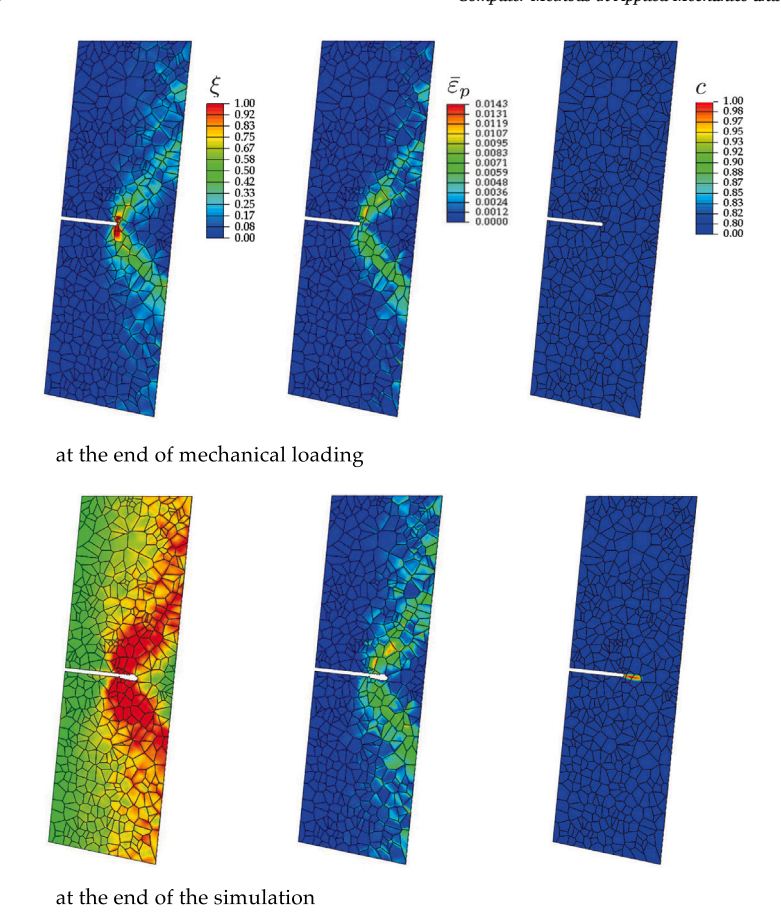


Fig. 10. Distribution of the martensite volume fraction,  $\xi$ , plastic strain accumulation,  $\bar{\epsilon}_n$ , and phase-field parameter, c, at the end of Simulation TM.

#### References

- [1] N. Morgan, Medical shape memory alloy applications The market and its products, Mater. Sci. Eng. A 378 (1) (2004) 16-23.
- [2] J.M. Jani, M. Leary, A. Subic, M.A. Gibson, A review of shape memory alloy research, applications and opportunities, Mater. Des. (1980-2015) 56 (2014) 1078–1113.
- [3] K. Gall, N. Yang, H. Sehitoglu, Y.I. Chumlyakov, Fracture of precipitated NiTi shape memory alloys, Int. J. Fract. 109 (1998) 189-207.
- [4] J. Olsen, Z. Zhang, H. Lu, C. van der Eijk, Fracture of notched round-bar NiTi-specimens, Eng. Fract. Mech. 84 (2012) 1-14.
- [5] J. Makkar, T. Baxevanis, Notes on the experimental measurement of fracture toughness of shape memory alloys, J. Intell. Mater. Syst. Struct. 31 (2019) 475–483
- [6] T. Baxevanis, D. Lagoudas, Fracture mechanics of shape memory alloys: Review and perspectives, Int. J. Fract. 191 (2015) 191-213.
- [7] Y. Freed, L. Banks-Sills, Crack growth resistance of shape memory alloys by means of a cohesive zone model, J. Mech. Phys. Solids 55 (2007) 2157–2180.
- [8] C. Maletta, F. Furgiuele, Analytical modeling of stress-induced martensitic transformation in the crack tip region of nickel-titanium alloys, Acta Mater. 58 (2010) 92–101.
- [9] T. Baxevanis, D. Lagoudas, A mode I fracture analysis of a center-cracked infinite shape memory alloy plate under plane stress, Int. J. Fract. 175 (2) (2012) 151–166.
- [10] T. Baxevanis, Y. Chemisky, D. Lagoudas, Finite element analysis of the plane strain crack-tip mechanical fields in pseudoelastic shape memory alloys, Smart Mater. Struct. 21 (2012) 094012.
- [11] G. Özerim, G. Anlaş, Z. Moumni, On crack tip stress fields in pseudoelastic shape memory alloys, Int. J. Fract. 212 (2) (2018) 205-217.
- [12] T. Baxevanis, C. Landis, D. Lagoudas, On the fracture toughness of pseudoelastic shape memory alloys, J. Appl. Mech. -T ASME 81 (2013) 041005.
- [13] D. Jiang, C. Landis, A constitutive model for isothermal pseudoelasticity coupled with plasticity, Shap. Mem. Superelasticity 2 (4) (2016) 360-370.
- [14] T. Baxevanis, A. Parrinello, D. Lagoudas, On the fracture toughness enhancement due to stress-induced phase in shape memory alloys, Int. J. Plast. 50 (2013) 158–169.
- [15] S. Jape, T. Baxevanis, D. Lagoudas, On the fracture toughness and stable crack growth in shape memory alloy actuators in the presence of transformation-induced plasticity, Int. J. Fract. 209 (2017) 117–130.
- [16] T. Baxevanis, C. Landis, D. Lagoudas, On the effect of latent heat on the fracture toughness of pseudoelastic shape memory alloys, J. Appl. Mech. Trans. ASME 81 (10) (2014) http://dx.doi.org/10.1115/1.4028191.
- [17] Y. You, X. Gu, Y. Zhang, Z. Moumni, G. Anlaş, W. Zhang, Effect of thermomechanical coupling on stress-induced martensitic transformation around the crack tip of edge cracked shape memory alloy, Int. J. Fract. 216 (1) (2019) 123–133.
- [18] M.Y. Alsawalhi, C.M. Landis, On the fracture toughness of shape memory alloys, Int. J. Fract. 236 (2) (2022) 201-218.
- [19] M.M. Hasan, T. Baxevanis, Structural fatigue and fracture of shape memory alloy actuators: Current status and perspectives, J. Intell. Mater. Syst. Struct. 33 (12) (2022) 1475–1486.

- [20] S. Jape, T. Baxevanis, D. Lagoudas, Stable crack growth during thermal actuation of shape memory alloys, Shap. Mem. Superelasticity 2 (1) (2016) 104–113.
- [21] A. Creuziger, L. Bartol, K. Gall, W. Crone, Fracture in single crystal NiTi, J. Mech. Phys. Solids 56 (9) (2008) 2896-2905.
- [22] G. Loughran, T. Shield, P. Leo, Fracture of shape memory CuAlNi single crystals, Int. J. Solids Struct, 40 (2) (2003) 271–294.
- [23] A. Azhdari, S. Nemat-Nasser, Hoop stress intensity factor and crack-kinking in anisotropic brittle solids, Int. J. Solids Struct. 33 (14) (1996) 2023-2037.
- [24] C. Miehe, M. Hofacker, F. Welschinger, A phase field model for rate-independent crack propagation: Robust algorithmic implementation based on operator splits, Comput. Methods Appl. Mech. Engrg. 199 (45–48) (2010) 2765–2778.
- [25] M. Borden, C. Verhoosel, M. Scott, T. Hughes, C. Landis, A phase-field description of dynamic brittle fracture, Comput. Methods Appl. Mech. Engrg. 217–220 (2012) 77–95.
- [26] M. Ambati, T. Gerasimov, L. De Lorenzis, A review on phase-field models of brittle fracture and a new fast hybrid formulation, Comput. Mech. 55 (2) (2014) 383-405.
- [27] M. Borden, T. Hughes, C. Landis, A. Anvari, I. Lee, A phase-field formulation for fracture in ductile materials: Finite deformation balance law derivation, plastic degradation, and stress triaxiality effects, Comput. Methods Appl. Mech. Engrg. 312 (2016) 130–166.
- [28] M. Ambati, T. Gerasimov, L. De Lorenzis, Phase-field modeling of ductile fracture, Comput. Mech. 55 (5) (2015) 1017-1040.
- [29] B. Talamini, M. Tupek, A. Stershic, T. Hu, J. Foulk, J. Ostien, J. Dolbow, Attaining regularization length insensitivity in phase-field models of ductile failure, Comput. Methods Appl. Mech. Engrg. 384 (2021) 113936.
- [30] J. Ulloa, J. Wambacq, R. Alessi, E. Samaniego, G. Degrande, S. François, A micromechanics-based variational phase-field model for fracture in geomaterials with brittle-tensile and compressive-ductile behavior, J. Mech. Phys. Solids 159 (2022) 104684.
- [31] S. Liu, Y. Wang, C. Peng, W. Wu, A thermodynamically consistent phase field model for mixed-mode fracture in rock-like materials, Comput. Methods Appl. Mech. Engrg. 392 (2022) 114642.
- [32] P. Ma, J. Ye, K. Tian, X. Chen, L. Zhang, Fracture phase field modeling of 3D stitched composite with optimized suture design, Comput. Methods Appl. Mech. Engrg. 392 (2022) 114650.
- [33] Z. Pan, L. Zhang, K. Liew, A phase-field framework for failure modeling of variable stiffness composite laminae, Comput. Methods Appl. Mech. Engrg. 388 (2022) 114192.
- [34] J. Wu, C. McAuliffe, H. Waisman, G. Deodatis, Stochastic analysis of polymer composites rupture at large deformations modeled by a phase field method, Comput. Methods Appl. Mech. Engrg. 312 (2016) 596–634.
- [35] E. Martínez-Pañeda, A. Golahmar, C. Niordson, A phase field formulation for hydrogen assisted cracking, Comput. Methods Appl. Mech. Engrg. 342 (2018) 742–761.
- [36] S. Lee, M. Wheeler, T. Wick, Pressure and fluid-driven fracture propagation in porous media using an adaptive finite element phase field model, Comput. Methods Appl. Mech. Engrg. 305 (2016) 111–132.
- [37] M. Hasan, T. Baxevanis, A phase-field model for low-cycle fatigue of brittle materials, Int. J. Fatigue 150 (2021) 106297.
- [38] P. Carrara, M. Ambati, R. Alessi, L. De Lorenzis, A framework to model the fatigue behavior of brittle materials based on a variational phase-field approach, Comput. Methods Appl. Mech. Engrg. 361 (2020) 112731.
- [39] A. Mesgarnejad, A. Imanian, A. Karma, Phase-field models for fatigue crack growth, Theor. Appl. Fract. Mech. 103 (2019) 102282.
- [40] G. Haveroth, M. Vale, M. Bittencourt, J. Boldrini, A non-isothermal thermodynamically consistent phase field model for damage, fracture and fatigue evolutions in elasto-plastic materials, Comput. Methods Appl. Mech. Engrg. 364 (2020) 112962.
- [41] Z. Khalil, A. Elghazouli, E. Martínez-Pañeda, A generalised phase field model for fatigue crack growth in elastic-plastic solids with an efficient monolithic solver, Comput. Methods Appl. Mech. Engrg. 388 (2022) 114286.
- [42] M. Simoes, E. Martínez-Pañeda, Phase field modelling of fracture and fatigue in shape memory alloys, Comput. Methods Appl. Mech. Engrg. 373 (2021) 113504.
- [43] M. Hasan, M. Zhang, T. Baxevanis, A finite-strain phase-field description of thermomechanically induced fracture in shape memory alloys, Shap. Mem. Superelasticity 8 (4) (2022) 356–372.
- [44] P. Shanthraj, B. Svendsen, L. Sharma, F. Roters, D. Raabe, Elasto-viscoplastic phase field modelling of anisotropic cleavage fracture, J. Mech. Phys. Solids 99 (2017) 19–34.
- [45] L. De Lorenzis, A. McBride, B.D. Reddy, Phase-field modelling of fracture in single crystal plasticity, GAMM-Mitt. 39 (1) (2016) 7-34.
- [46] M. Diehl, M. Wicke, P. Shanthraj, F. Roters, A. Brueckner-Foit, D. Raabe, Coupled crystal plasticity—phase field fracture simulation study on damage evolution around a void: Pore shape versus crystallographic orientation, JOM, J. Miner., Met. Mater. Soc. (TMS) 69 (2017) 872–878.
- [47] C.A. Hernandez Padilla, B. Markert, A coupled ductile fracture phase-field model for crystal plasticity, Contin. Mech. Thermodyn. 29 (2017) 1017–1026.
- [48] S. Na, W. Sun, Computational thermomechanics of crystalline rock, Part I: A combined multi-phase-field/crystal plasticity approach for single crystal simulations, Comput. Methods Appl. Mech. Engrg. 338 (2018) 657–691.
- [49] X. Zhuang, S. Zhou, G. Huynh, P. Areias, T. Rabczuk, Phase field modeling and computer implementation: A review, Eng. Fract. Mech. 262 (2022) 108234.
- [50] B. Haghgouyan, C. Hayrettin, T. Baxevanis, I. Karaman, D. Lagoudas, Fracture toughness of NiTi-Towards establishing standard test methods for phase transforming materials, Acta Mater. 162 (2019) 226–238.
- [51] K.F. Hane, T. Shield, Microstructure in the cubic to monoclinic transition in titanium-nickel shape memory alloys, Acta Mater. 47 (9) (1999) 2603-2617.
- [52] T. Ezaz, J. Wang, H. Sehitoglu, H. Maier, Plastic deformation of NiTi shape memory alloys, Acta Mater. 61 (1) (2013) 67-78.
- [53] T. Simon, A. Kröger, C. Somsen, A. Dlouhy, G. Eggeler, On the multiplication of dislocations during martensitic transformations in NiTi shape memory alloys, Acta Mater. 58 (5) (2010) 1850–1860.
- [54] K. Otsuka, X. Ren, Physical metallurgy of Ni-Ti-based shape memory alloys, Prog. Mater. Sci. 50 (5) (2005) 511-678.
- [55] M. Hossain, T. Baxevanis, A finite strain thermomechanically-coupled constitutive model for phase transformation and (transformation-induced) plastic deformation in NiTi single crystals, Int. J. Plast. 139 (2021) 102957.
- [56] M. Cherkaoui, M. Berveiller, H. Sabar, Micromechanical modeling of martensitic transformation induced plasticity (TRIP) in austenitic single crystals, Int. J. Plast. 14 (7) (1998) 597–626.
- [57] C. Yu, G. Kang, Q. Sun, D. Fang, Modeling the martensite reorientation and resulting zero/negative thermal expansion of shape memory alloys, J. Mech. Phys. Solids 127 (2019) 295–331.
- [58] M. Zhang, T. Baxevanis, Tailoring the anisotropic (positive/zero/negative) thermal expansion in shape memory alloys through phase transformation and martensite (re) orientation, Internat. J. Engrg. Sci. 177 (2022) 103687.
- [59] J. Monroe, D. Gehring, I. Karaman, R. Arroyave, D.W. Brown, B. Clausen, Tailored thermal expansion alloys, Acta Mater. 102 (2016) 333-341.
- [60] M.E. Gurtin, Generalized Ginzburg-Landau and Cahn-Hilliard equations based on a microforce balance, Physica D 92 (3-4) (1996) 178-192.
- [61] M.-X. Wagner, W. Windl, Lattice stability, elastic constants and macroscopic moduli of NiTi martensites from first principles, Acta Mater. 56 (20) (2008) 6232–6245.
- [62] H. Amor, J.-J. Marigo, C. Maurini, Regularized formulation of the variational brittle fracture with unilateral contact: Numerical experiments, J. Mech. Phys. Solids 57 (8) (2009) 1209–1229.
- [63] C. Miehe, F. Welschinger, M. Hofacker, Thermodynamically consistent phase-field models of fracture: Variational principles and multi-field FE implementations, Internat. J. Numer. Methods Engrg. 83 (10) (2010) 1273–1311.

- [64] N.P. van Dijk, J.J. Espadas-Escalante, P. Isaksson, Strain energy density decompositions in phase-field fracture theories for orthotropy and anisotropy, Int. J. Solids Struct. 196 (2020) 140–153.
- [65] C. Kuhn, A. Schlüter, R. Müller, On degradation functions in phase field fracture models, Comput. Mater. Sci. 108 (2015) 374-384.
- [66] L. Svolos, J. Plohr, G. Manzini, H. Mourad, On the convexity of phase-field fracture formulations: Analytical study and comparison of various degradation functions, Int. J. Non-Linear Mech. (2023) 104359.
- [67] R.J. Geelen, Y. Liu, T. Hu, M.R. Tupek, J.E. Dolbow, A phase-field formulation for dynamic cohesive fracture, Comput. Methods Appl. Mech. Engrg. 348 (2019) 680–711.
- [68] J.-Y. Wu, A unified phase-field theory for the mechanics of damage and quasi-brittle failure, J. Mech. Phys. Solids 103 (2017) 72-99.
- [69] D. Peirce, R. Asaro, A. Needleman, An analysis of nonuniform and localized deformation in ductile single crystals, Acta Metall. 30 (6) (1982) 1087-1119.
- [70] T. Gerasimov, L. De Lorenzis, A line search assisted monolithic approach for phase-field computing of brittle fracture, Comput. Methods Appl. Mech. Engrg. 312 (2016) 276–303.
- [71] T. Wick, Modified Newton methods for solving fully monolithic phase-field quasi-static brittle fracture propagation, Comput. Methods Appl. Mech. Engrg. 325 (2017) 577-611.
- [72] A. Kopaničáková, R. Krause, A recursive multilevel trust region method with application to fully monolithic phase-field models of brittle fracture, Comput. Methods Appl. Mech. Engrg. 360 (2020) 112720.
- [73] P.K. Kristensen, E. Martínez-Pañeda, Phase field fracture modelling using quasi-Newton methods and a new adaptive step scheme, Theor. Appl. Fract.
- [74] T.K. Mandal, V.P. Nguyen, J.-Y. Wu, C. Nguyen-Thanh, A. de Vaucorbeil, Fracture of thermo-elastic solids: Phase-field modeling and new results with an efficient monolithic solver. Comput. Methods Appl. Mech. Engrg. 376 (2021) 113648.
- [75] R. Bharali, S. Goswami, C. Anitescu, T. Rabczuk, A robust monolithic solver for phase-field fracture integrated with fracture energy based arc-length method and under-relaxation, Comput. Methods Appl. Mech. Engrg. 394 (2022) 114927.
- [76] I. Cormeau, Numerical stability in quasi-static elasto/visco-plasticity, Internat. J. Numer. Methods Engrg. 9 (1) (1975) 109-127.
- [77] D. Peirce, C.F. Shih, A. Needleman, A tangent modulus method for rate dependent solids, Comput. Struct. 18 (5) (1984) 875-887.
- [78] J. Wu, Y. Huang, Comprehensive implementations of phase-field damage models in Abaqus, Theor. Appl. Fract. Mech. 106 (2020) 102440.
- [79] K. Gall, M.L. Dunn, Y. Liu, P. Labossiere, H. Sehitoglu, Y.I. Chumlyakov, Micro and macro deformation of single crystal NiTi, J. Eng. Mater. Technol. 124 (2) (2002) 238–245.
- [80] O. Matsumoto, S. Miyazaki, K. Otsuka, H. Tamura, Crystallography of martensitic transformation in Ni–Ti single crystals, Acta Metall. 35 (8) (1987) 2137–2144.
- [81] K. Gall, H. Sehitoglu, The role of texture in tension-compression asymmetry in polycrystalline NiTi, Int. J. Plast. 15 (1) (1999) 69-92.
- [82] N. Siredey, E. Patoor, M. Berveiller, A. Eberhardt, Constitutive equations for polycrystalline thermoelastic shape memory alloys.: Part I. Intragranular interactions and behavior of the grain, Int. J. Solids Struct. 36 (28) (1999) 4289–4315.
- [83] I. Beyerlein, C. Tomé, A dislocation-based constitutive law for pure Zr including temperature effects, Int. J. Plast. 24 (5) (2008) 867-895.
- [84] B. Bourdin, G. Francfort, J. Marigo, The variational approach to fracture, J. Elasticity 91 (1) (2008) 5-148.
- [85] A. Illiopoulos, J. Steuben, T. Kirk, T. Baxevanis, J. Michopoulos, D. Lagoudas, Thermomechanical failure response of notched NiTi coupons, Int. J. Solids Struct. 125 (2017) 265–275.
- [86] T. Baxevanis, A. Parrinello, D. Lagoudas, On the driving force for crack growth during thermal actuation of shape memory alloys, J. Mech. Phys. Solids 89 (2016) 255–271.